1 **MOF-metal nanohybrid-assisted charge transfer amplification for electrochemical**

2 **biosensing of MUC1 Cancer Biomarker**

3 Sarita Devi[a], Shivangi Goel[a], Sonia Rani[a], Rudolf J. Schneider[b,c], Rishika Rohilla[a], Surbhi

4 Kumari[a], and Nirmal Prabhakar[a]*

5

6 [a]Department of Biochemistry, Panjab University, Chandigarh, India, 160014

7 [b]Bundesanstalt für Materialforschung und -prüfung (BAM), Department of Analytical

8 Chemistry; Reference Materials, Richard-Willstätter-Str. 11, 12489 Berlin, Germany

9 [c]Technische Universität Berlin, Straße des 17. Juni 135, 10623 Berlin, Germany
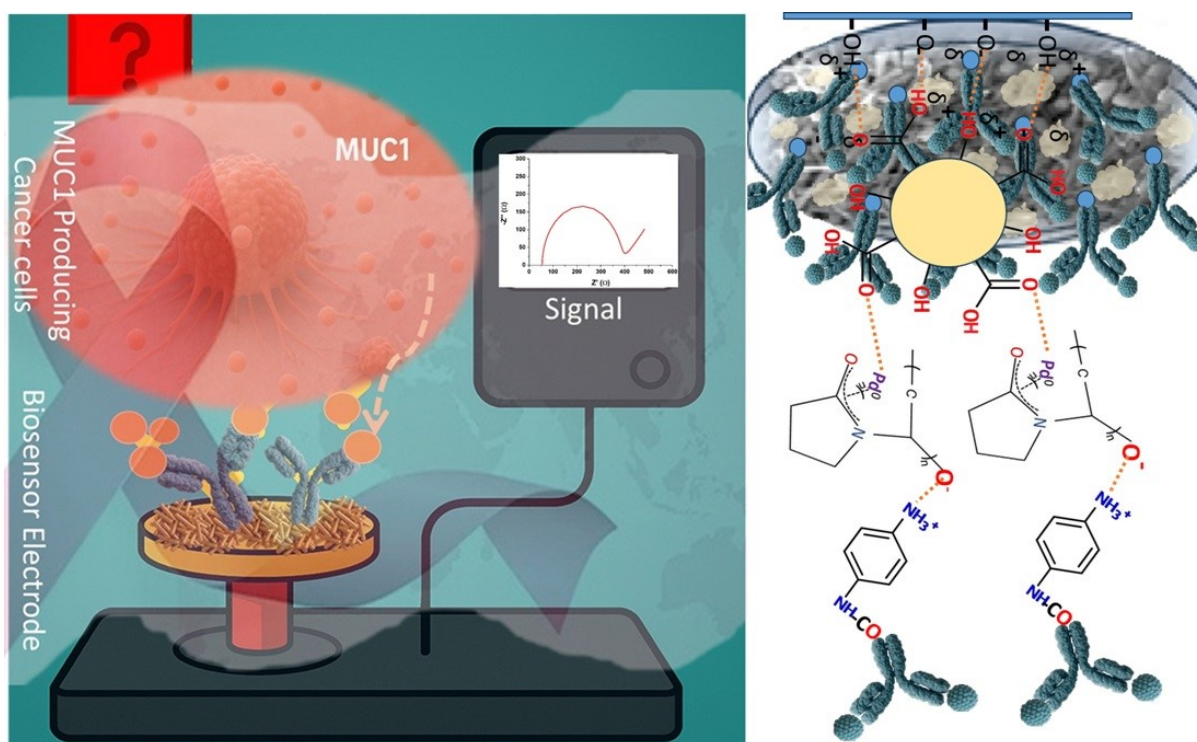
10

11 *Corresponding author:

12 Nirmal Prabhakar - Department of Biochemistry, BMS Block-2, Panjab University, Sector 25,
13 Chandigarh, India, 160014. E-mail: nirmalprabhakar@gmail.com

14

15

16

17 **Graphical Abstract:**

18

Materials

Palaldium (II) chloride (PdCL$_2$), 6-mercapto-1-hexanol (MCH), N-ethyl-N´-(3-dimethylaminoprpyl) carbodiimide hydrochloride (EDC), N, N-dimethylformamide (DMF), N- hydroxysuccinimide (NHS), 2-(N-morpholino) ethanesulfonic acid (MES), sulphuric acid (H$_2$SO$_4$), hydrochloric acid (HCl), isopropyl alcohol (C$_3$H$_8$O), tetrahydroxy-1,4-benzoquinone hydrate (THQ), terephthalic acid (TPA), iron (II) sulfate heptahydrate (FeSO$_4$·7H$_2$O), anti MUC-1 mAb and human serum (H4522-20mL) were purchased from sigma-aldrich. Iron (III) chloride hexahydrate (FeCl$_3$·6H$_2$O) was bought from fluka. Sodium hydroxide (NaOH), potassium chloride (KCl), sodium chloride (NaCl), sodium phosphate monobasic monohydrate (NaH$_2$PO$_4$.H$_2$O), disodium hydrogen phosphate anhydrous (Na$_2$HPO$_4$), potassium ferricyanide [K$_3$Fe (CN)$_6$], potassium chloride (KCl), potassium ferrocyanide [K$_4$Fe (CN)$_6$.3H$_2$O], polyvinylpyrrolidone (PVP) and bovine serum albumin (BSA) were purchased from HiMedia. Acetone and N-Methyl-2-Pyrrolidone (NMP) were procured from Sisco Research Laboratories Pvt. Ltd. (SRL), Mumbai, India. Potassium iodide (KI) and Glacial acetic acid were supplied by merck. Mumbai, India and Rankem, India respectively. 1,4-Phenylenediamine (PDA) was manufactured by Tokyo Chemical Industry Co., Ltd. Japan. MUC-1 protein was sought from Biolynx, China. Hepcidin and holo-transcobalamin (holo TC) were taken from Real-Gene Labs. Ethanol was from Compagnie Sucrière Sénégalaise (CSS) reagents. Insulin was manufactured by Lilly USA. The fluorine tin oxide doped (FTO) glass sheet was bought from sigma-aldrich and cut in the dimension of 4 cm × 0.6 cm (L x W) prior to use. Autoclaved water (resistivity 18.2 MΩ/cm at 25°C) was used throughout the study. The preparation steps of all the reagents, used to carry out the study, are mentioned supplementary information.

Reagents preparation

Hydroxylation of FTO was performed by electrodeposition of NaOH (1 M) solution. It was prepared by adding 1.6 g of NaOH to 40 ml DI water and sonicated for 10 min, later stored at room temperature (RT). 50 mM Phosphate buffer (PB) (pH 6.0) was used for electrolyte (Fe (CN)$_6$]$^{3-/4-}$) preparation. 1.42 g Na$_2$HPO$_4$ and 1.56 g NaH$_2$PO$_4$.H$_2$O were added in 200 ml DI water and sonicated for 5 min. The pH of the PB buffer was adjusted to 6.0 using HCl (100 mM) and NaOH (100 mM). The electrolyte solution was prepared by mixing 0.16 g [K$_3$Fe (CN)$_6$], 0.21 g [K$_4$Fe (CN)$_6$.3H$_2$O] and 0.74 g KCl in 100 ml of autoclaved PB (50 mM, pH 6.0). The washing buffer (100 mM PB, pH 7.2-7.3) was prepared by adding Na$_2$HPO$_4$ (0.71 g) and NaH$_2$PO$_4$.H$_2$O (0.78 g) in 50 ml DI water. This buffer solution was used for the washing of modified-FTO during conjugation and preparation of biosensing surface. PB (10 mM, pH

52 7.2-7.3) was used for analyte preparation. It was prepared by mixing 0.071 g Na_2HPO_4, 0.069

53 g $Na_2HPO_4.2H_2O$, 3.9 mg NaCl (1.34 mM) and 10.2 mg KCl (2.74 mM) in 50ml DI water. The

54 pH was adjusted to 7.2-7.3 using HCl (100 mM) and NaOH (100 m M). This buffer solution

55 was utilized for MUC1 preparation during detection. FTO cleaning reagents includes: (i) 1%

56 Acetic acid, 1 ml of acetic acid (17.4 M) solution to 100 ml DI water, (ii) 70% Ethanol: 70 ml

57 of 100% ethanol to 30 ml of DI water, and (iii) 0.1 M H_2SO_4: 99.456 ml of 18.38 M H_2SO_4 to

58 99.456 ml DI water. MES buffer (0.1 M, pH 5-6) was prepared by adding the 0.196 g of MES

59 in 10 ml DI water and utilized for the activation of antiMUC1 mAbs through EDC/NHS

60 mediated carbodiimide coordination chemistry. For the same, the EDC solution (0.333 mM)

61 and NHS (0.984 mM) were prepared in MES buffer. All the solutions and reagents were freshly

62 prepared during each modification step and experimentation.

63 The detailed optimized protocol for electrochemical characterization of FTOs at each modification step

64 is as follow. Prior to use, the FTO electrodes were cleaned in the bath sonicater using 1% acetic acid

65 for 30 minutes, followed by the 70% ethanol and DI water. Finally, these electrodes were washed with

66 0.1 M H_2SO_4 and dried in oven. The cleaned FTOs were hydroxylated by electrodeposition method

67 using NaOH (1 M) through chronoamperometry. The parameters used for chronoamperometry were

68 finalized as -1.25 V for 500 sec. After hydroxylation, the FTOs were dried at RT. Later, 10μl of the

69 optimized FeMOF@PdNR/PDA solution was drop casted and spread uniformly on the FTO-OH and

70 dried for 1 hour in oven at 60°C. Subsequently, the 10 μl of activated antiMUC1 mAb (0.6 μg/ml) was

71 dropped on it and incubated in humid chamber for the optimized period. Subsequently, the modified

72 FTOs (FeMOF@PdNR/PDA/antiMUC1Ab) were washed with PB and dried at RT. The possible vacant

73 surface at FTO/FeMOF@PdNR/PDA/ntiMUC1mAb were blocked by 10 μl MCH (2 mM). After drying

74 at RT for 15 minutes, the final biosensor electrode (FTO/FeMOF@PdNR/PDA/antiMUC1Ab/MCH)

75 was used for analyte detection by EIS, CV and DPV techniques. The modified FTOs were scanned from

76 -1 to 3.0 V at different scan rates.

77 **Characterization studies**

78 Various modifications, done on FTO electrode surface, were characterized using various

79 techniques to confirm successful development of the biosensor. A potentiostat/galvanostat

80 (Autolab, Metrohm: model no.: 302NFRA32M) was used for electrochemical analysis using a

81 standard three-electrode setup; Fourier Transform Infrared (FT-IR) spectroscopy (Perkin

82 Elmer, Spectrum II) for functional chemical characterization; field emission scanning electron

83 microscopy (FE-SEM) for morphological analysis; and X-ray diffraction (XRD was used for

84 structural changes validation. For UV–Visible spectroscopy (Ultrospec 7000), 1 mL of each

85 sample was monitored in the range of 200–800 nm to evaluate the electronic transitions and
86 confirm the successive surface modifications of the nanocomposites.

87 EIS analysis was performed using Frequency Response Analyzer (FRA) technique within 0.1-
88 10^5 Hz frequency range with an excitation potential of 10 mV at an open circuit potential (OCP)
89 of 0.23 V. A redox couple of equimolar concentration $Fe(CN)_6^{3-/4-}$ (5mM) in 0.1 M PBS/KCl
90 (pH   6)   employing   a   three-electrode   system,   with
91 FTO/FeMOF@PdNR/PDA/antiMUC1Ab/MCH as the WE, Ag/AgCl as the reference
92 electrode, and counter platinum electrode was used for measurements. The EIS data was
93 analysed using Nyquist plot, and the equivalent circuit ([R(C[RW])]) was fitted to find the
94 charge transfer resistance (R_{ct}) value. For comprehensive analysis of electrochemical
95 robustness and dielectric response of the modified-FTO interface, the CV and DPV were
96 carried out in the extended potential window from –1 V to +3 V. The data was statistically
97 analyzed using the OriginPro 8 software.
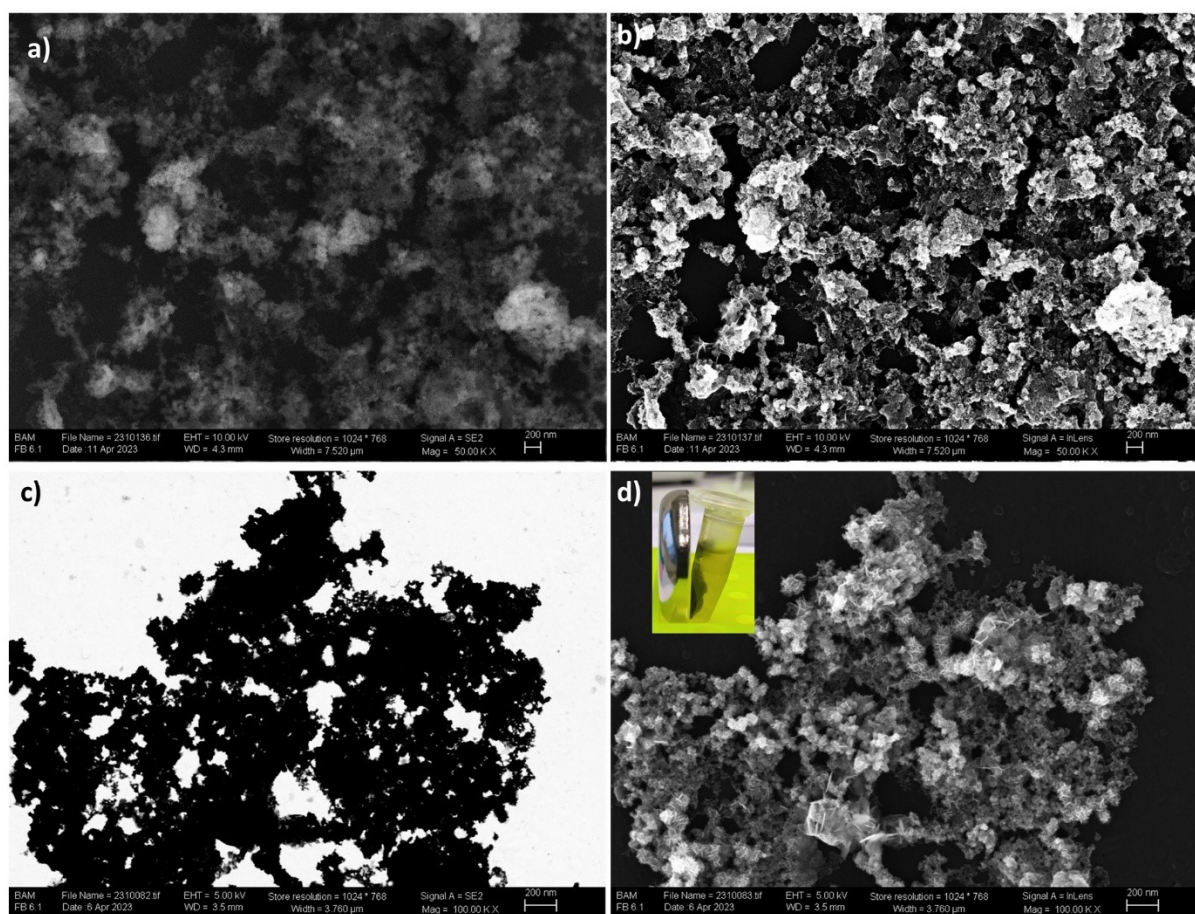
98

99

100

101

102

103

104

105

106

107

108

109

110

111

Results and Discussion

Figure S1: FESEM images of as-synthesized FeMOF: (a) and (c) The morphological characteristics of the FeMOF on the Si-wafer and net, respectively (both were captured by the detector SE2), are shown, revealing their size distribution in nanometers and identifiable morphology; (b) and (d) a visibly more enhanced view of the nanostructures (on Si-wafer and net, respectively with distinct shape (both were captured by the detector InLens). [Details (a) and (b: EHT 10.00 kV, WD 4.3 mm, store resolution 1024*768, width 7.520 μm, magnification 50.00 KX, scale bar 200 nm]. [Details (c) and (d): EHT 5.00 kV, WD 3.5 mm, store resolution 1024*768, width 3.760 μm, magnification 100.00 KX, scale bar 200 nm]. [Inset of d): The magnetic behavior of FeMOF in the presence of an external magnet].

The SEM images of the FEMOF on silicon wafers and net substrates, as obtained with SE2 and InLens detectors are presented in **Figure S1**. The assembled-MOF nanostructures highlight the interconnected particles with a dimension around 100 nm. It suggests that the dense lamellae were integrated in the synthetic FeMOF and contribute to the large specific surface area exposing plenty active sites and high bioreceptor loading potential. The morphology of the MOF via different substrates (net) and detectors concorded with this interpretation. The magnetic property of FeMOF was confirmed with the help of an external magnet (inset of figure S1d).
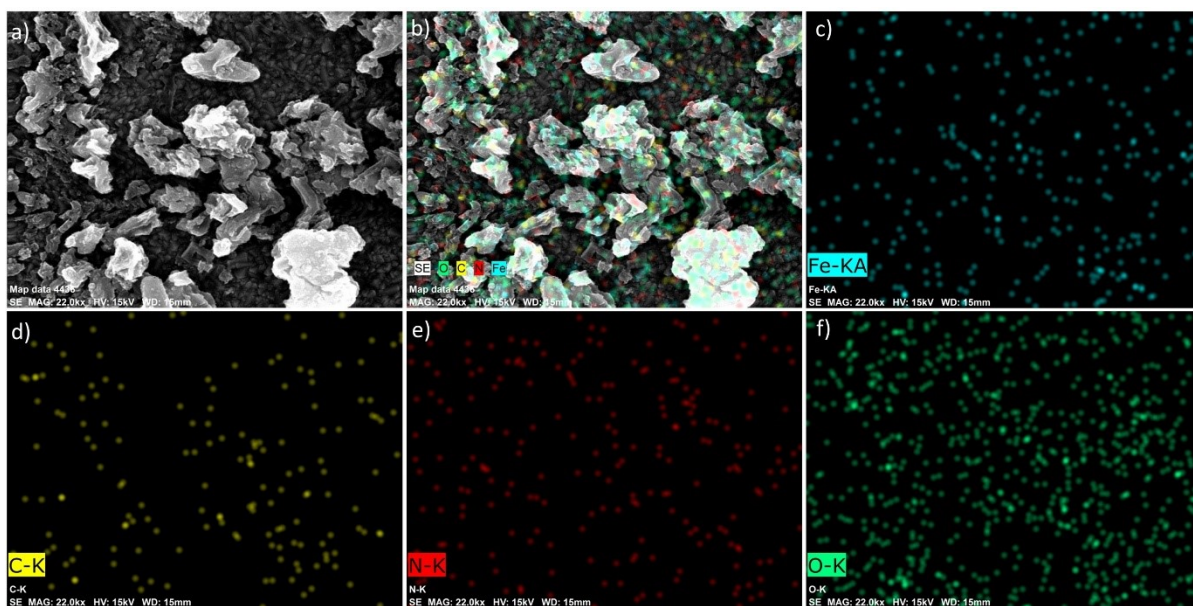
Figure S2: SEM image of the FeMOF shown with the selected as-marked area for (a) EDS measurement (5 kV), and (b) elemental mapping. (c to f) Elemental mapping data of FeMOF.
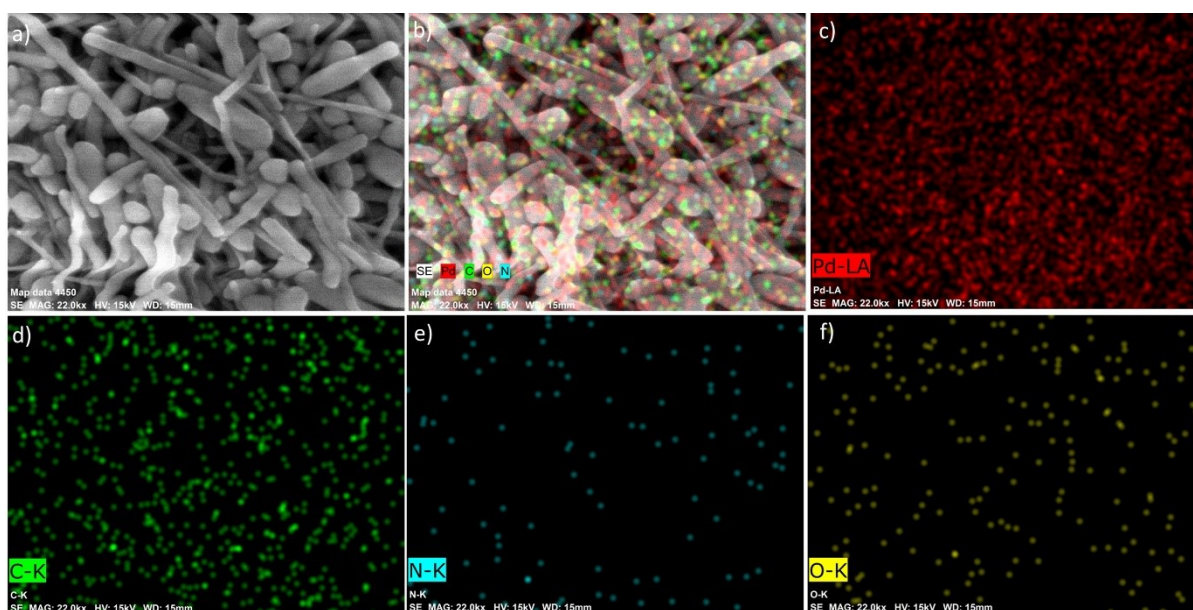
Figure S3: SEM image of the PdNR shown with the selected as-marked area for (a) EDS measurement (5 kV), and (b) elemental mapping. (c to f) Elemental mapping data of PdNR.

Figure S4: SEM image of the FeMOF@PdNR shown with the selected as-marked area for (a) EDS measurement (5 kV), and (b) elemental mapping. (c to g) Elemental mapping data of FeMOF@PdNR.
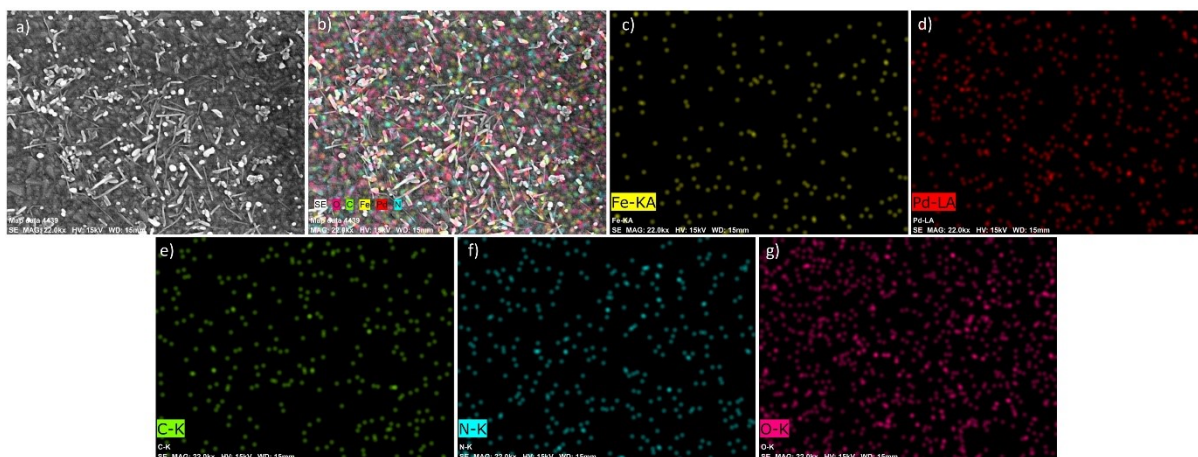

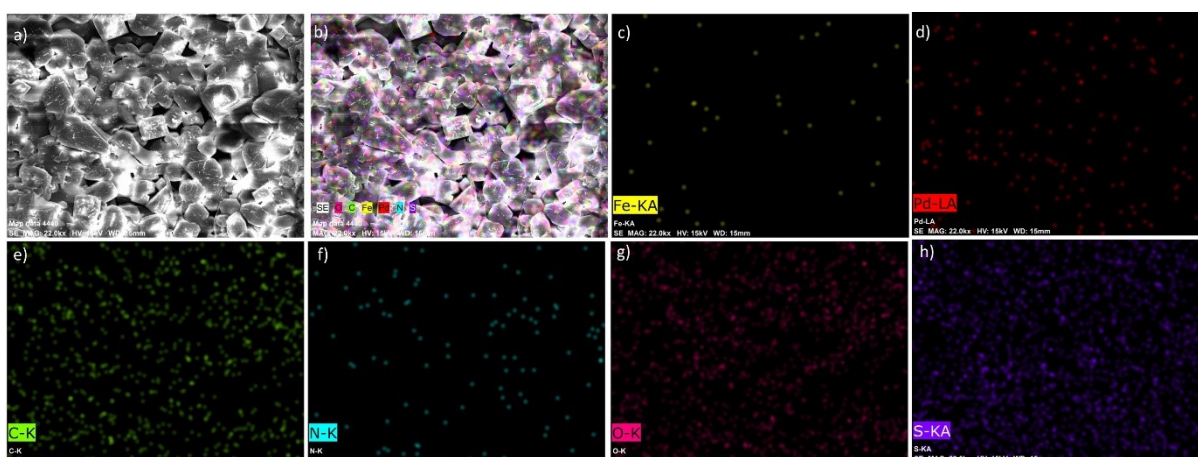
Figure S5: SEM image of the FeMOF@PdNR/PDA/antiMUC1Ab shown with the selected as-marked area for (a) EDS measurement (5 kV), and (b) elemental mapping. (c to h) Elemental mapping analysis of FeMOF@PdNR/PDA/antiMUC1Ab.
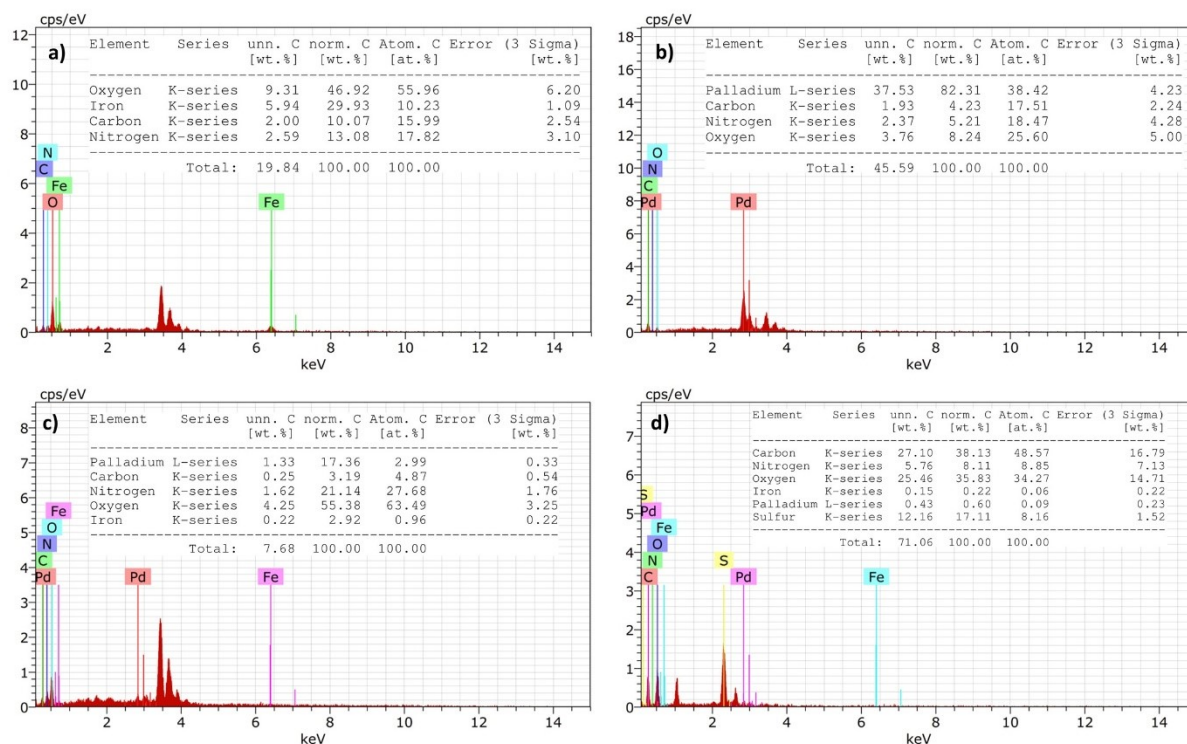
Figure S6: SEM-EDS (5 kV) spectra and elemental composition tables (insets) as obtained from the selected as-marked SEM areas of the (a) FeMOF, (b) PdNR, (c) FeMOF@PdNR, and (d) FeMOF@PdNR/PDA/antiMUC1Ab.

Figure S7: The hydrodynamic size of FeMOF and PdNRs was determined using the dynamic light-scattering technique.

Dynamic light scattering (DLS)

DLS analysis, as shown in **figure S7,** revealed the single peak of FeMOF particles showing the uniform sized particles. While PdNRs display 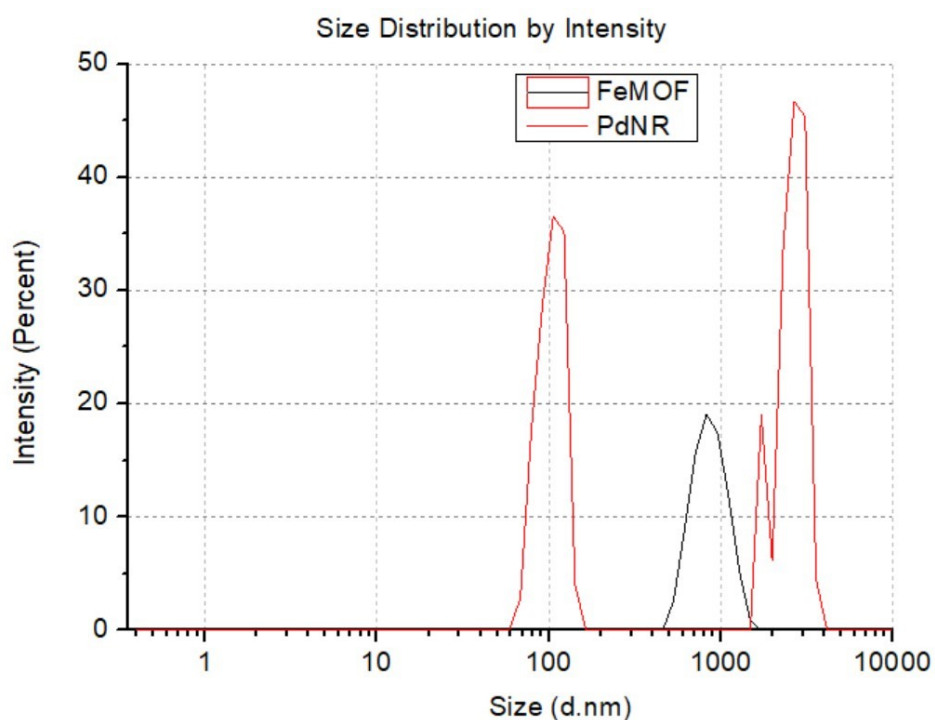two distinct peaks owing to the length and breadth of rods as ~2870 nm and ~98 nm, respectively. The intense dual peaks indicate a bimodal size distribution reflecting their rod-like shape and associated aggregates.

UV-Visible absorption spectroscopy

The absorption spectrum of FeMOF (**Figure S8a**) reveals the π–π* and n- π* transitions at ~220 nm and ~330 nm that confirms the presence of aromatic ligand frameworks, TPA and THQ. The most intense absorption band between 430–460 nm is assigned to a strong ligand-metal charge transfer (LMCT) transition, confirming the Fe^{3+} as dominant oxidation state, and Fe^{3+} as the primary metal center. The weak band beyond 600 nm is typical of Fe^{3+}-based materials but does not dominate[1].
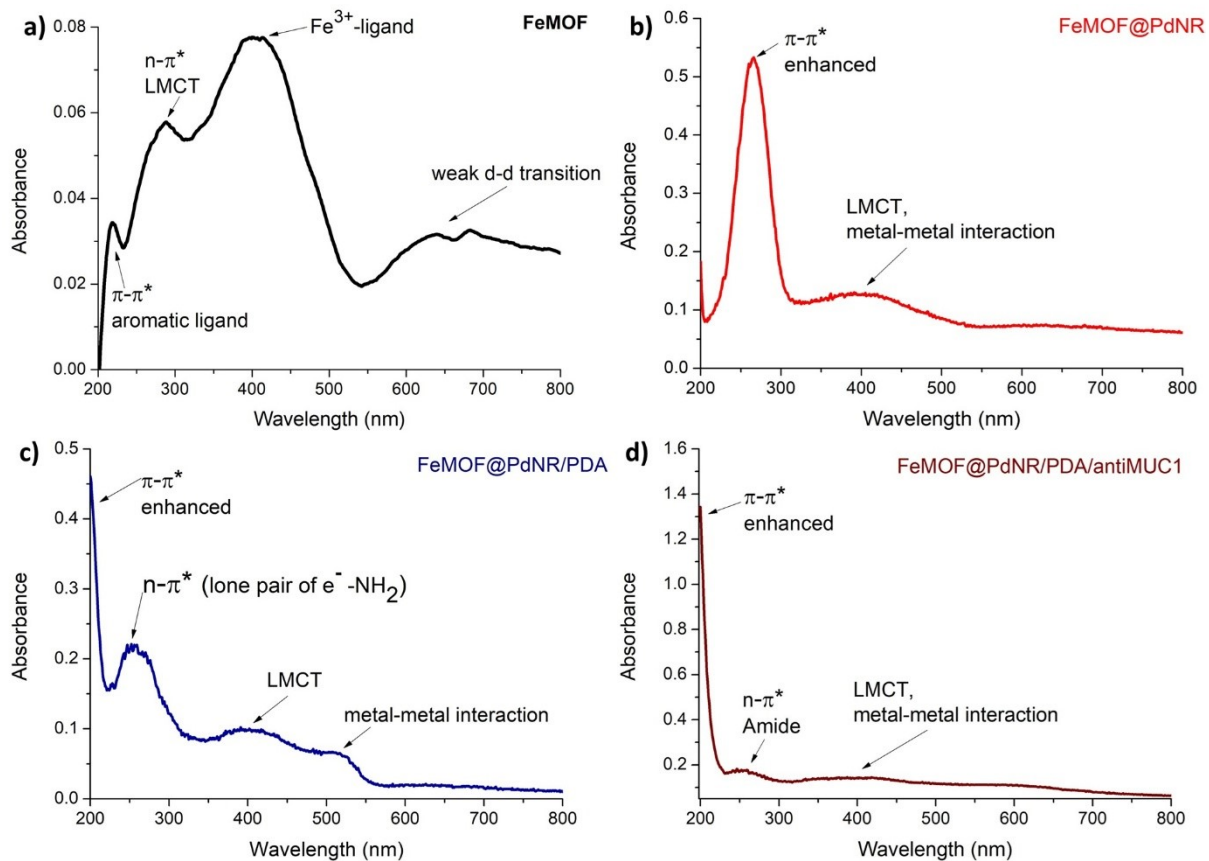
Figure S8: The UV-visible absorption spectra (wavelength range: 200- 800 nm) of the nanomaterials at each synthesis and conjugation step: FeMOF (a), FeMOF@PdNR (b), FeMOF@PdNR/PDA (c) and FeMOF@PdNR/PDA/antiMUC1Ab (d).

The absorption spectrum of FeMOF@PdNR reveals notable changes compared to the bare FeMOF, indicating successful integration of PdNRs and corresponding alterations in the electronic structure (**Figure S8b**). A strong absorption peak around 260–270 nm, with significantly higher intensity than

173 that of the original FeMOF, suggests the enhanced π–π* transitions is might be due to strong interaction
174 between PVP-stabilized PdNRs and the aromatic ligands of FeMOF. Also, the broad shoulder (320 to
175 500 nm) is ascribed to the LMCT transitions and possible metal–metal interactions between Fe and Pd
176 species. These spectral features indicate the possible lowering in effective band gap, resulting in
177 enhanced conductivity[2]. The absorption spectrum of the FeMOF@PdNR/PDA (**Figure S8c**) shows a
178 sharp and intense peak at 210–220 nm, that is attributed to π–π* transitions of the aromatic rings of
179 FeMOF ligands. A secondary hump in the 270–290 nm region corresponds to n–π* transitions, possibly
180 due to the lone pair electrons of –NH_2 or –OH groups to π* orbitals, suggesting strong conjugation. A
181 broad and flattened band from at higher wavelength is the characteristic of LMCT, particularly from
182 ligands to Fe^{3+} centers or PdNRs[3]. In the absorption spectrum of FeMOF@PdNR/PDA/antiMUC1Ab
183 (**Figure S8d**), an enhanced peak between 200–220 nm is attributed to increased π–π* transitions from
184 PDA and other aromatic components, along with contributions from amide bonds and peptide
185 backbones of the antibody. The shoulder at 270–290 nm corresponds to n–π* transitions, primarily from
186 amide groups in the antibody, as well as possible absorption from tryptophan and tyrosine residues,
187 which are abundant in protein structures. In the 300–600 nm range, the spectrum displays a band due to
188 the sustained Fe–ligand and Pd interactions[4]. These studies indicate the successful conjugation and
189 immobilization of respective material.

190 **Table S1:** The FTIR peak assessment of FeMOF, PdNR and FeMOF@PdNR.

Material	Peaks (cm^{-1})	Interpretation
FeMOF	3658	Presence of – OH groups on FeMOF surface[5].
	2977, 2888	Due to -C-H symmetrical stretching vibrations[6].
	630	Related to Fe-O bond vibration[7].
	824	Corresponds to stretching vibrations of bound hydrogen[8].
	1382	Attributed to C-O stretching of TPA carbonate ions[6].
	1536	Assigned to stretching vibrations for carbonyl groups[9].
	1661	Mark of the unsaturated conjugated double bond of quinones[6].
PdNRs	2888, 2977	Presence of –CH_2– groups of PVP[10].
	608	Attributed to Pd–O stretching[11].
	830	Stretching vibrations of bound hydrogen[8].
	1146, 1770	Indicates C-O stretching from PVP[12].
FeMOF@PdNR	2848 – 2977	Combined features, intensified alkyl C–H stretching[13].
	1046	Represent the C–H in-plane bending[14].
	1192, 1729	Indicates C-O stretching from organic linkers[12, 15].

191

192

193
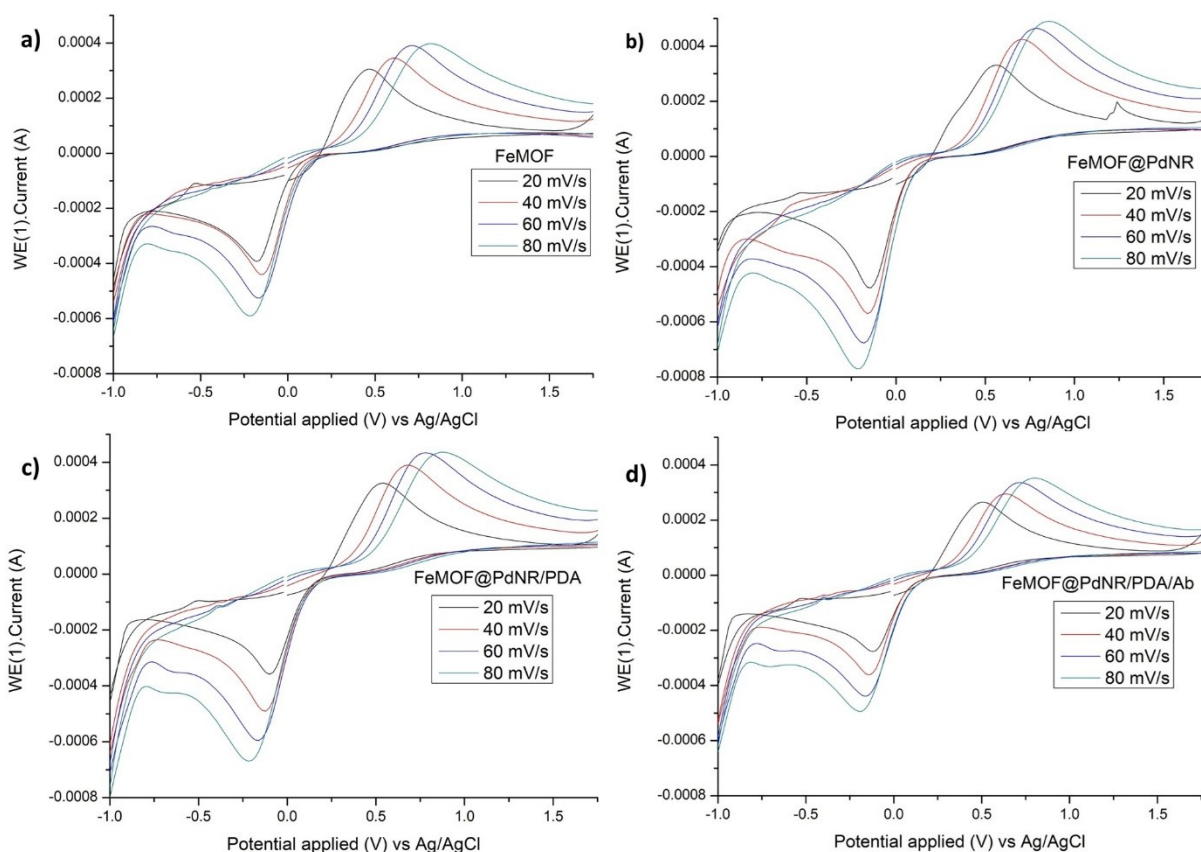
Figure S9: Cyclic voltammetry carried out using the modified FTO electrodes as working electrodes with the (a) FeMOF, (b) FeMOF@PdNR, (c) FeMOF@PdNR/PDA, and (d) FeMOF@PdNR/PDA/antiMUC1Ab in 5 mM $K_3[Fe(CN)_6]^{3-/4-}$ equipped vs Ag/AgCl reference electrode, at scan rates 20, 40, 60, and 80, mV/s.

**Table S2:** Electroactive surface area and related parameters of modified-FTOs at various steps.

Working electrode	Residual Sum of Squares	Adj. R-Square	Intercept	Standard Error	Slope	Standard Error	A_{eff} cm²
Bare FTO Ia	7.88E-13	0.9853	1.36E-05	1.33E-06	8.48E-05	5.95E-06	**1.60E-03**
Bare FTO Ic	6.57E-12	0.9667	-8.89E-06	3.84E-06	-1.61E-04	1.72E-05	
FTO/FeMOF Ia	2.09E-10	0.9444	2.08E-04	2.17E-05	7.00E-04	9.70E-05	**1.89E-01**
FTO/FeMOF Ic	1.81E-10	0.9911	-1.21E-04	2.02E-05	-0.00165	9.01E-05	
FTO/FeMOF@PdNR Ia	5.34E-10	0.9450	1.83E-04	3.46E-05	0.00112	1.55E-04	**3.02E-01**
FTO/FeMOF@PdNR Ic	6.06E-10	0.9811	-1.76E-04	3.69E-05	-0.00207	1.65E-04	
FTO/FeMOF@PdNR/PDA Ia	5.50E-10	0.8965	2.19E-04	3.52E-05	8.17E-04	1.57E-04	**2.20E-01**
FTO/FeMOF@PdNR/PDA Ic	1.33E-10	0.9963	-4.92E-05	1.73E-05	-0.00221	7.75E-05	
FTO/FeMOF@PdNR/PDA/antiMUC1Ab Ia	1.25E-10	0.9612	1.71E-04	1.67E-05	6.50E-04	7.48E-05	**1.75E-01**
FTO/FeMOF@PdNR/PDA/antiMUC1Ab Ic	8.02E-11	0.9952	-6.41E-05	1.34E-05	-0.00151	6.01E-05	

199

200

Scan rate in PBS

Figure S10 shows the CV data of the bare FTO **(Figure S10a)**, FTO/FeMOF (at different y-scale to compare with bare **(Figure S10b)** and PdNR modified FTO/FeMOF **(Figure S10c))** and FTO/FeMOF@PdNR (**Figure S10d**) in PBS at varying scan rate (0.02 V/s to 0.14 V/s).
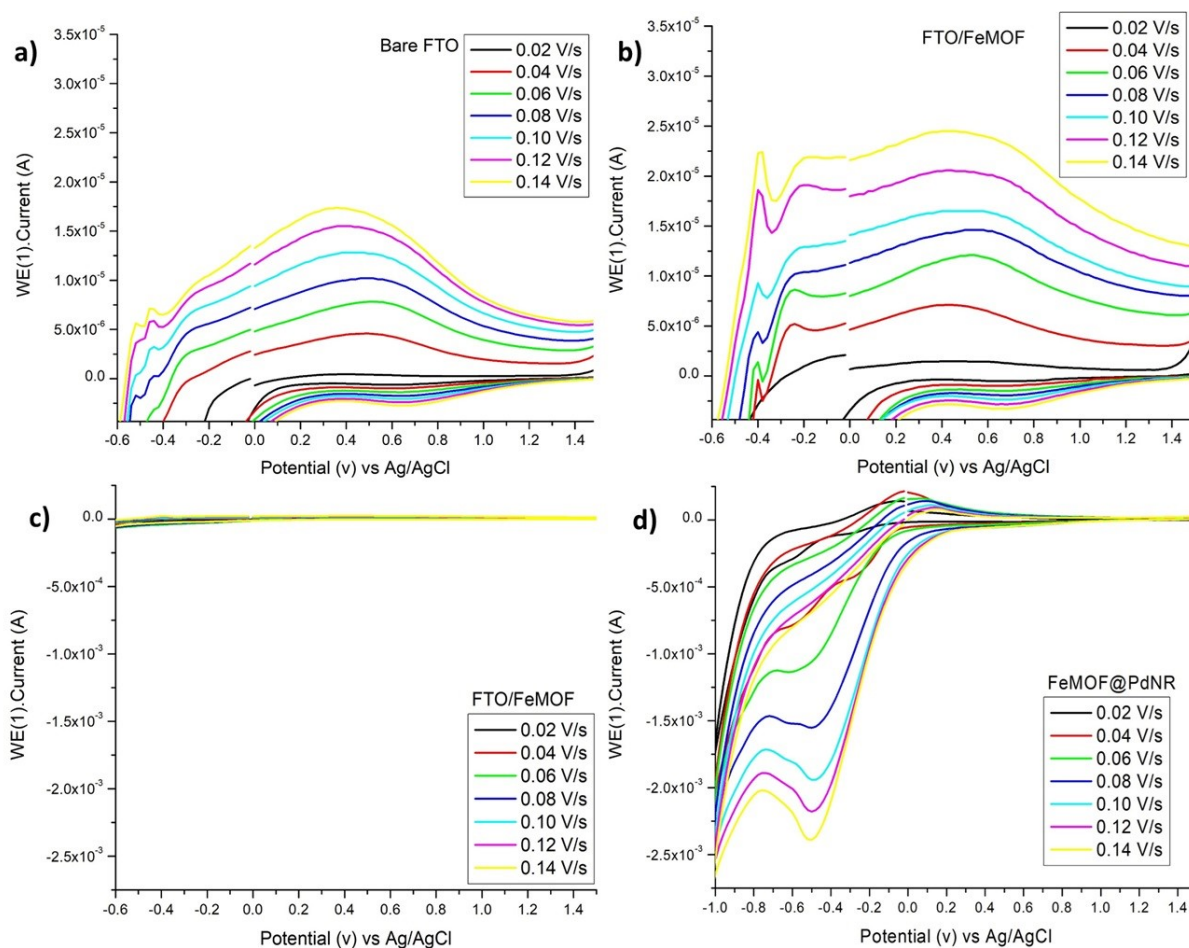
Figure S10: Cyclic voltammetry was carried out using the (a) bare FTO, (b) FTO/FeMOF, and (d) FTO/FeMOF@PdNR, in PBS equipped vs Ag/AgCl reference electrode, at scan rates of 0.02 to 0.14 V/s. (c) CV data of FTO/FeMOF demagnified at the same current range (y-scale) to that of FTO/FeMOF@PdNR (shown in (d), to compare efficiently with their outcomes.

The bare FTO delivers insignificant current, only the capacitive background, across the potential window with the subtle faradaic peaks, due to the inert electrode substrate. After FeMOF deposition, the evident increase in both the anodic and cathodic currents is observed, due to the higher A_{eff} and redox-active sites. As the peak currents increase with increase in scan rate, it is consistent with the diffusion-limited access of the redox probe through the film. FTO/FeMOF@PdNR delivers the largest faradaic currents overall and most defined-peaks which are intensified with increase in scan rate. The highly prominent reduction peak (E_{pc} 0.5 V) indicates the impact of PdNR's conductive and catalytic properties. PdNRs markedly improved the A_{eff} and charge transfer kinetics of FTO/FeMOF surface.

Optimization Studies

FTO-Hydroxylation

The Nyquist plot (**Figure S11a**), current variation (**Figure S11e**), and the DPV curves (**Figure S11i**) represents the impedance and conductive properties of untreated (non-hydroxylated), but cleaned FTO (black) and hydroxylated FTO (red), both later modified with FeMOF in DMF. The FeMOF deposited on the untreated FTO exhibits a high Rct value and lower current generation as-compared to the one, deposited on FTO-OH. It specifies that the FeMOFs are attached more efficiently onto the FTO-OH surface, on account of the stronger interaction (H-bonding) than that of the weak electrostatic interaction with the untreated FTO. Therefore, all the further WE fabrications were done on hydroxylated-FTOs.
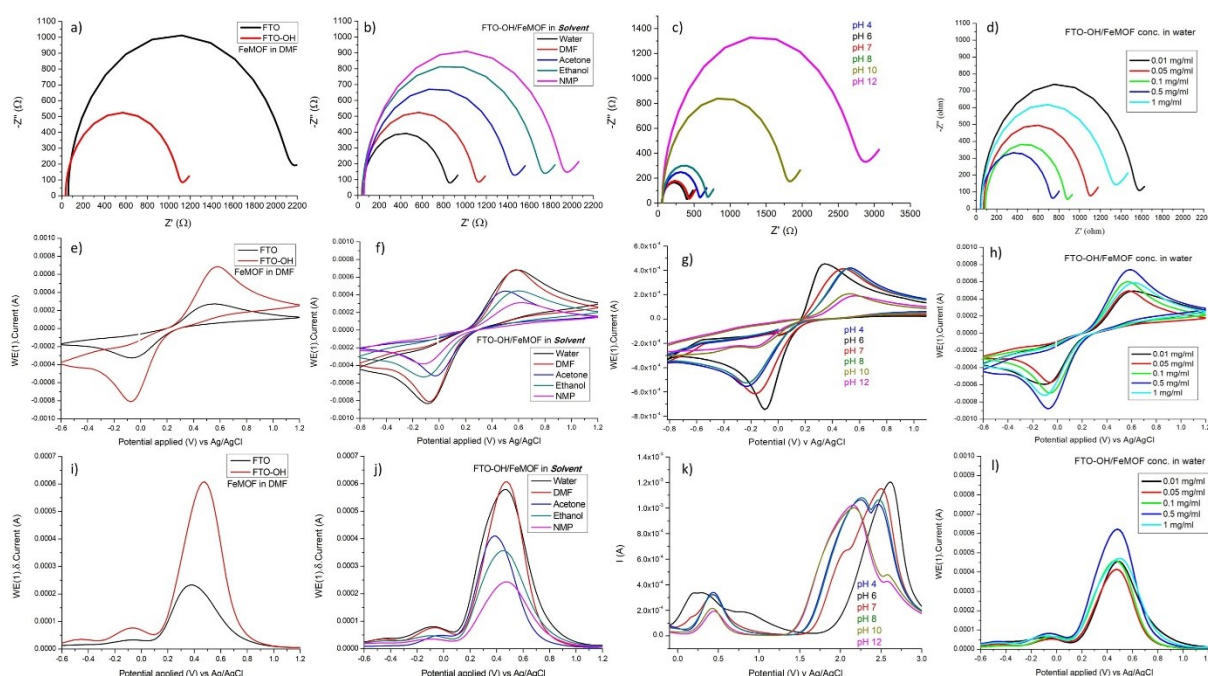
Figure S11: The electrochemical properties of FTO-working electrodes, as-recorded using EIS (a-d), CV (e-h), and DPV (i-l) techniques for the optimization of the parameters: FTO-hydroxylation, solvent for FeMOF, electrolyte pH, and FeMOF concentration on FTO, respectively, to achieve the best performing WE surface.

Solvent optimization

The effect of different solvents (e.g. ethanol, DMF, NMP, acetone and water) on the EC performance of the FTO/FeMOF is shown in **figures S11b, S11f, and S11j**. However, the water and DMF led to relatively better film formation and dispersion stability compared to other solvents, resulting in comparably similar I_{pa} but, the impedance (Rct) obtained in DMF was significantly higher. Therefore, water was selected as the optimal solvent for further studies.

Electrolyte pH

Alterations in pH may lead to change in charge distribution, redox behavior and interactions at the fabricated electrode surface. **Figures S11c, S11g, and S11k** show that the electrochemical performance of FTO–OH/FeMOF is highly dependent on electrolyte pH. Among the values (pH 4 to 12), the lowest impedance and higher conductivity is observed at pH 6, highly favoring the electron transfer process. In contrast, the performance decreases significantly at higher pH levels (especially pH 10 and 12), likely due to FeMOF instability or surface degradation[16].

FeMOF concentration Optimization

The FeMOF concentration, to be used during electrode modification, has a direct impact on the density, thickness, and uniformity of the deposited layer, which in turn influences the sensor's electrochemical behavior. To investigate this, FeMOF was tested at various concentrations (0.01, 0.05, 0.1, 0.5 and 1 mg/ml in water) onto FTO-OH (**Figure S11d, S11h, and S11l**). At lower concentrations, the Rct remains high and conductivity low, due to insufficient surface coverage. At concentration, 0.5 mg/ml FeMOF, a noticeable decrease in Rct and elevation in I_{pa} as well as current amount in DPV were observed, suggesting the optimum surface coverage for better electron transfer. Beyond this concentration, the abundant particle coverage results in hinderance of electron transfer. Hence, the optimal 0.5 mg/ml FeMOF is selected for further studies.
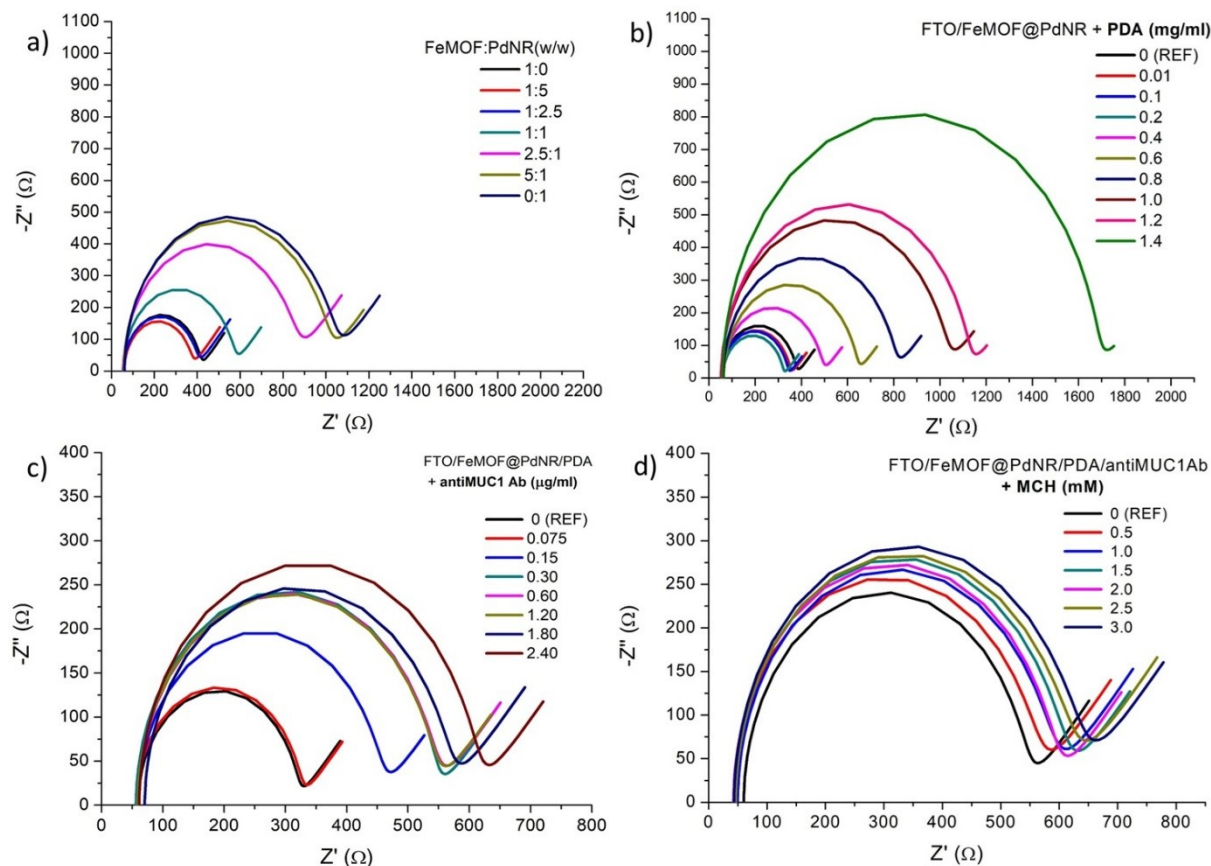
FeMOF@PdNRs concentration optimization

Nyquist plots from EIS (**Figure S12a**) show that the effect of FeMOF:PdNR composition on the electrochemical characteristics during WE fabrication. It can be observed that the 1:5:: FeMOF:PdNRs (w/w) composite exhibits the lowest impedance value, consequently the highest I_{pa} (**Figure S13a**) and the current at 0.4 V (**Figure S14a**), indicating excellent conductivity. Here, the PdNRs are likely well-integrated within the FeMOF framework, forming a continuous structure that facilitates efficient electron movement. Composites with higher FeMOF content (e.g., 2.5:1, 5:1) tend to show more resistance, as FeMOF alone offers comparatively less efficient electron transport. In contrast, when the PdNRs content is too high (e.g., 1:2.5, 0:1), it might not have been incorporated well onto the FTO surface leading to uneven electron flow[17]. Thus, the 1:5::FeMOF:PdNR (w/w) ratio offers a balanced matrix for improved electrochemical performance.

PDA concentration optimization

In order to achieve the uniform surface coverage, the optimal PDA concentration was determined from a range of its concentrations (1.4, 1.2, 1, 0.8, 0.6, 0.4, 0.2, 0.1 and 0.01 mg/ml). From **figure S12b**, it can be observed that the 0.2 mg/ml PDA is required to achieve the well-organized layer on FTO/FeMOF@PdNRs, as evident from the lowest Rct and higher current data (**Figure S13b and S14b**).

272 However, at concentrations beyond 0.2 mg/ml, the excessive PDA led to possible steric hindrance[18].
273

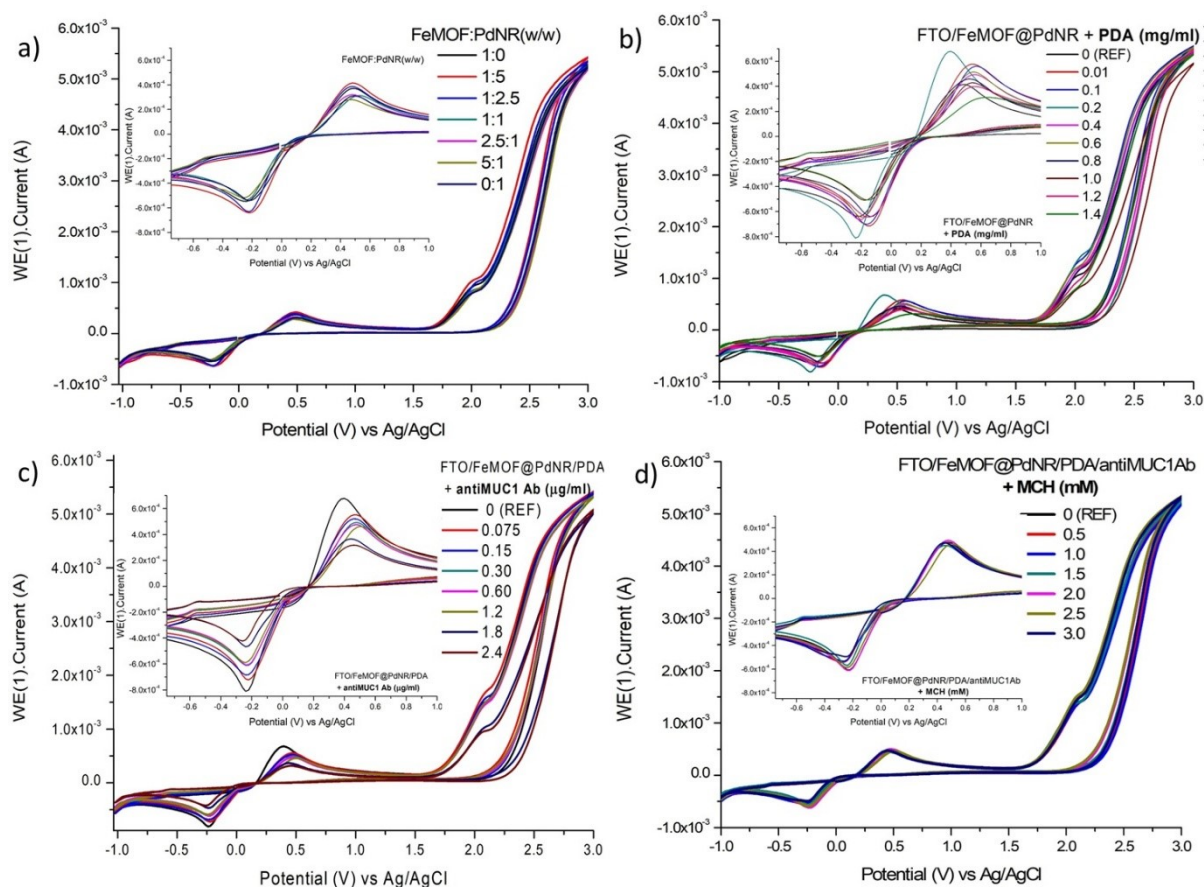**Figure S12:** EIS data: The variation in impedance of FTO-working electrodes, as-recorded using EIS technique for the optimization of: a) FeMOF:PdNR concentration, b) PDA concentration to be used for FTO/FeMOF@PDNR surface treatment, c) antiMUC1 Ab concentration, as-required for optimum immobilization onto FTO/FeMOF@PdNR/PDA surface, and d) the MCH concentration for efficient blocking of possible-free sites onto FTO/FeMOF@PdNR/PDA/antiMUC1Ab surface.

Anti-MUC1 Ab concentration

A robust and detectable electrochemical signal from an immunosensor is produced by effective hybridization with the analyte, which is ensured by the adequate bioreceptor immobilization to the sensor surface. Generally, challenges like nonspecific binding or inadequate signal production can result from the extremely high or low antiMUC1 Ab concentrations, respectively. Therefore, the different concentrations of AntiMUC1 Ab (2.4, 1.8, 1.2, 0.6, 0.3, 0.15 and 0.075 µg/ml) were incubated on FTO/FeMOF@PdNRs/PDA electrode and evaluated (**Figure S12c, S13c and S14c**). Nyquist curves as well as the current characteristics show that the antibodies result in the decrease in electrochemical conductivity, mainly owing to the insulating behavior of these large biomolecules. This trend is

290 followed up to 0.6 µg/ml anti-MUC1 Ab and saturated beyond that, which might be due to the non-
291 specific multilayer buildup. Therefore, it is interpreted that the 0.6 µg/ml antiMUC1 Ab provide the
292 adequate surface immobilization.

293

294 **Figure S13:** CV data. The variation in I_{pa} and I_{pc} of FTO-working electrodes, as-recorded using CV
295 technique for the optimization of: a) FeMOF:PdNR concentration, b) PDA concentration to be used for
296 FTO/FeMOF@PDNR surface treatment, c) antiMUC1 Ab concentration, as-required for optimum
297 immobilization onto FTO/FeMOF@PdNR/PDA surface, and d) the MCH concentration onto
298 FTO/FeMOF@PdNR/PDA/antiMUC1Ab surface.

MCH concentration optimization

300 The Ab-modified FTO were further treated with MCH, ranging from 0.5 mM to 3 mM. **Figures S12d,**
301 **and S13d** show that there is no such remarkable change in the conductivity of biosensor electrode in
302 presence of varying MCH. Although, a significant improvement is evident at 1 mM MCH, that can be
303 ascribed to the effective blocking of unoccupied sites while maintaining charge transfer capability. The
304 adverse effect of higher MCH concentration on the electrochemical properties of
305 FTO/FeMOF@PdNRs/PDA/antiMUC1Ab surface, is evident form the DPV curves shown in **Figure**
306 **S14d.**
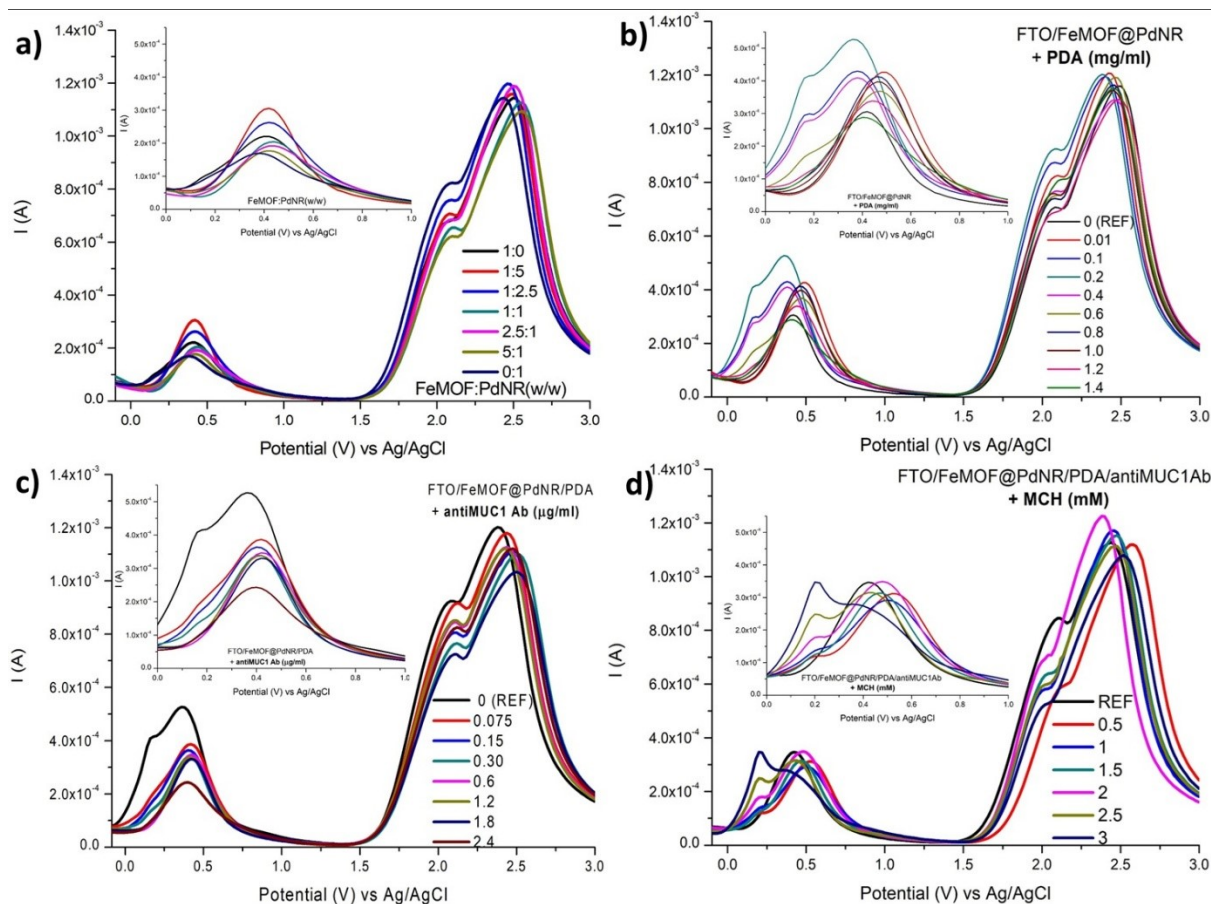
Figure S14: DPV data. The electrochemical properties of FTO-working electrodes, as-recorded using DPV technique for the optimization of: a) FeMOF:PdNR concentration, b) PDA concentration to be used for FTO/FeMOF@PDNR surface treatment, c) antiMUC1 Ab concentration, as-required for optimum immobilization onto FTO/FeMOF@PdNR/PDA surface, and d) the MCH concentration for efficient blocking of possible-free sites onto FTO/FeMOF@PdNR/PDA/antiMUC1Ab surface.

Extended potential window in CV and DPV profiling

The current output at higher anodic potential (>1.5 V) is affected by significant physio-chemical transitions and is required for mapping of maximum electrochemical stability window (ESW). While the conventional redox region of $[Fe(CN)_6]^{3-/4-}$ is limited within the potential window -0.5 V to +1.0 V vs Ag/AgCl, further extending it to 3.0 V can provide the critical information about the electrochemical resilience, dielectric breakdown threshold and faradaic/non-faradaic behavior (or pseudocapacitance) of the engineered electrode interface.

Here, in **figures S13 and S14,** the extended CV and DPV analysis of each modified FTO surface is provided. The deviations from the baseline capacitive current above 2.0 V and the appearance of broad anodic polarization currents (1.5 V to 3.0 V region) is highly important as it shows the involvement of functional properties of FeMOF@PdNR hybrid i.e MOF-lattice polarization, ligand field distortion or Pd-OH intermediate formation, that results in electron-hopping and high-density surface states,

S17

eventually in the signal-amplification ability of modified electrode. The resultant pseudocapacitive behavior is ascribed to the surface-confined redox transitions or metal-oxygen interactions at high potentials. As the ESW measurement is mandatory for biosensors intended for clinical translation due to the possibility of oxidative interference in real serum samples. Thereby, this extended analysis eliminated the chances of any parasitic oxidation peaks from organic linker PDA, antibody layer or blocking molecules and confirms the absence of polymeric or biomolecular degradation up to 3.0 V. It shows the chemical inertness and antifouling property of the bio-interface.

Unlike most biosensor platforms that fail due to the oxidative degradation above 1.2 V, this FeMOF@PdNR hybrid retained structural integrity and exhibited reversible high-field electroactivity up to high voltage range. It indicates the exceptional robustness suitable for aggressive potential pulsing protocols, long-term biosensing cycles and repeated regeneration in complex clinical matrices.

Response Time

The analyte, MUC1, was allowed to interact with the sensor electrode surface for 30 minutes at interval of 5 minutes, as shown in **figure S15.** The plot shows % change in electrochemical signals (Rct from EIS, Ipa from CV, and I from DPV) vs. response time (0–30 min) for the MUC1 biosensor. It can be observed that the highest relative change in Rct (~180–190%) occurred in the first 10 minutes, thereafter it reaches a plateau. Similarly, the current responses also increase to maximum within the first 10 minutes but with lower magnitude (~20–30% change), then stabilize. This observation indicates that 10 min. were sufficient for antigen–antibody binding, and no further significant antigen capture occurs.
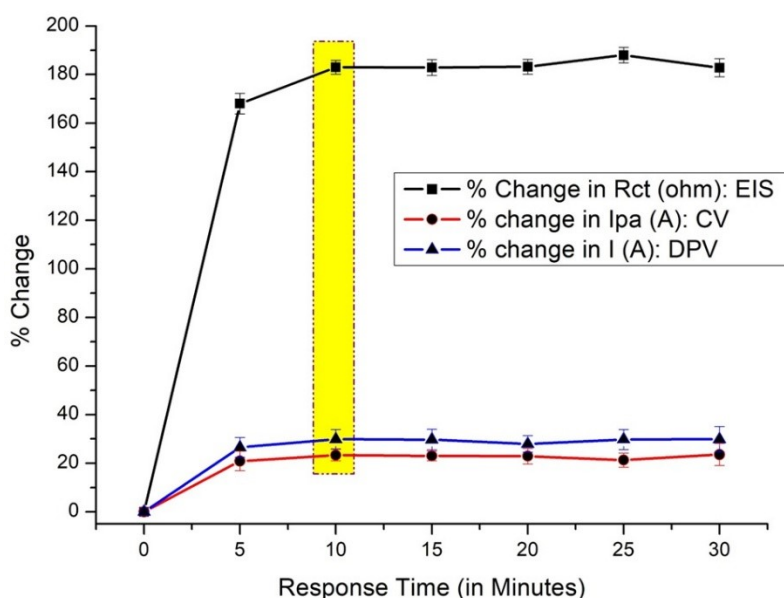
Figure S15: The response time optimization for MUC1 interaction with antiMUC1 Ab resulted in a stable signal after 10 minutes of incubation.

Bode Plot assessment

In the Bode magnitude plot (log Z vs log f), as shown in **Figure 5a**, the lowest overall impedance of FTO/FeMOF indicates the good conductivity rendered to FeMOF film. After intercalation with PdNR, there is a further reduction in the impedance, that confirms that the PdNRs enhance the electron transfer via catalytic ad conductive pathways. Even after the treatment with PDA, minute but considerable effect on the overall impedance can be observed, that might be due to the addition of polymeric coating and creating a partial conductive layer, while also providing the binding sites for antibodies. The major alteration in impedance is visible after the immobilization of antibodies, the insulating biomolecule, as it hinders the charge transfer at the electrode/electrolyte interface. The highest Z-value, before analyte addition, is noticed after MCH addition, further restricting electron tunnelling [19]. The final MUC1 detection (both in buffer and serum samples) is achieved as evident form the abrupt and strong increase in impedance, reflecting successful Ag-Ab binding which further restricts electron transfer. Although, minor nonspecific adsorptions are expected in serum samples, due to different ionic strength, and matrix effects that alter interfacial charge distribution.

Moreover, the Bode phase plot (Phase vs log f), is presented in **Figure 5b.** Phase close to $-90°$ indicates capacitive dominance, while phase near $0°$ indicates resistive dominance, therefore, the low phase angle is a characteristic of resistive/conductive behaviour of surface [19]. It is slightly shifted to higher phase ($42°$) after the incorporation of PdNR into FTO/FeMOF surface and later PDA treatment, indicating more capacitive contribution due to larger electroactive surface area. After the Abs immobilization and MCH blocking, the progressive increase in phase maximum (70–$80°$) and broadening in the phase peak, represented the dominance of capacitive/insulating layers and more homogeneous but resistive interface. The phase maximum shifts upward and broadens after MUC1 binding, confirming biomolecular adsorption leading to higher dielectric contribution and slower interfacial kinetics. The magnitude and phase data further corelates the impedance and voltammetry results shown in **Figure 6**.

Assessment of the electrochemical properties of Biosensor electrode surface

Figure 6 is a compilation for the final proposed FTO-based biosensor platform, as-prepared based on the optimized parameters. From the Nyquist plots of all modified states **(Figure 6a)**, it is evident that the semicircle diameters, Rct, initially reduced after the PdNR introduction. Later, each organic/biomolecular layer raises the Rct, showing their interfacial insulating character, mediated-steric hindrance and slower electron transfer. The low-frequency Warburg tail (second arc) becomes progressively more pronounced after biomodification, indicating the mass-transport/diffusion limitations and interrupted capacitance due to non-uniform film and insulating layers.

The mechanistic decomposition i.e. kinetic vs mass-transfer control and a typical Nyquist-plot with circuit interpretation are shown in **Figure 6b and 6c**. A typical kinetic-controlled region is interpreted

from the left semicircle at high-mid frequency region, while the mass-transfer controlled region from right hand extension at mid-low frequency [19]. The smaller inner semicircle at high-to-mid frequencies corresponds to Rct and Cdl showing that the PdNR decoration accelerates the heterogeneous kinetics. However, the right-hand extension (45° line/Warburg behaviour) indicates the diffusion- limited transport of redox species to the electrode surface. The characteristic frequency relationship is shown by the annotated $\omega \approx 1/(R2 \cdot Cdl)$ relation, representing the frequency where the transition between kinetic and mass-transfer control happens. After antibody immobilization **(Figure 6c),** the admittance parameter (Y0) or constant phase element (CPE) exponent, that models non-ideal capacitance, likely decreases showing that the system becomes more non-ideal. This indicates formation of a thicker, heterogeneous biomolecular layer that restricts charge transfer and introduces distributed capacitance. MCH effectively fills the hydrophobic gaps, creating a more complete insulating monolayer as evident form the variation in Y0. Therefore, the EIS measurements can be concluded as the incremental Rct and the evolution of capacitive behaviour (from ideal Cdl to CPE-like) are precisely the measurable transducers for impedimetric biosensing. The fitted circuit values (R, C or Y0, Warburg) are shown in **table S3**. R1 value being <100 Ω (~40–60 Ω) is showing the stable electrolyte conditions, also the higher Y0 suggests stronger diffusion contributions, while lower Y0 indicates more surface-controlled kinetics. Lower χ^2 indicates a better fit. Here, the χ^2 values (~0.9–9.3) shows good fit.

Table S3: The fitted circuit [R(C[RW])] values derived from Nyquist plot for modified working electrode.[1]

Working Electrode	R1 (Ω)	R2 (Ω)	W(Y0) (mMho)	Cdl (μF)	χ^2	i_o (μAcm^{-2})	K_{app} (cm s^{-1})
FTO/FeMOF	43.3	659	8.79	11.9	0.90747	108.3	2.24 x 10^{-4}
FTO/FeMOF@PdNR	60.1	308	6.48	6.97	7.7591	231.7	4.8 x 10^{-4}
FTO/FeMOF@PdNR/PDA	59.6	257	12.3	6.28	8.4085	277.7	5.75 x 10^{-4}
FTO/FeMOF@PdNR/PDA/ antiMUC1Ab	60.4	476	7.75	6.32	8.2729	150	3.1 x 10^{-4}
FTO/FeMOF@PdNR/PDA/ antiMUC1Ab/MCH	49.8	526	5.92	7.42	9.2615	135.7	2.81 x 10^{-4}

Figure 6d and 6e show the voltametric characteristics. The respective parameters are summarized in **table S4**. The moderately large redox peak separation, ΔE, in FTO/FeMOF CV, indicates the quasi-reversible electron transfer. The modest signal baseline in its DPV curve can be ascribed to the conductive FeMOF active sites yet still moderate Rct. The increased I$_{pa}$, I$_{pc}$ and slightly decreased ΔE of FTO/FeMOF@PdNR CV, and increase peak current in DPV is due to the improved electron transfer kinetics and catalytic activity of PdNR. The highest I$_{pa}$, I$_{pc}$ and reduced ΔE of FTO/FeMOF@PdNR/PDA CV provides the better reversibility of redox reaction. Additionally, the

[1]R1: solution resistance, R2: charge transfer resistance (Rct) at an electrode surface, W: Warburg element accounting for mass transfer phenomena of diffusion of species in electrochemical system, *Cdl*: double-layer capacitance at the same interface, χ^2 – Chi-Square, a statistical measure that shows the goodness of fit of an equivalent circuit to the experimental EIS data, i$_o$: exchange current density, K_{app}: apparent electron transfer rate constant.

generation of two distinct oxidation peaks with strong signal in DPV cab be credited to the abundant amine/quinone groups enhancing the interfacial charge transfer. These split peaks indicate the multiple redox-active processes between FeMOF and PDA functional groups. In the CV spectrum of FTO/FeMOF@PdNR/PDA/antiMUC1Ab, there is a sharp drop in I_{pa}, and I_{pc} as well as the widening of ΔE, which is supported by the reduction of current in DPV data. Eventually, the biosensor electron fabrication end-process depends on the MCH introduction, which results in further ΔE elevation and the slowest kinetics so far. DPV technique evidently resolves the multi-step processes.

Table S4: The voltametric current and potential parameters of modified-FTO at various steps.

| Working Electrode	CV					DPV		I^* (mol cm^{-2})
	I_a (A)	I_c (A)	E_{pa} (V)	E_{pc} (V)	ΔE (V)	E (V)	I (A)	
FTO/FeMOF	3.66E-4	-5.4E-4	0.489	-0.239	0.728	0.41	2.21E-4	2.17E-11
FTO/FeMOF@PdNR	4.18E-4	-6.4E-4	0.485	-0.221	0.706	0.42	3.05E-4	2.47E-11
FTO/FeMOF@PdNR/ PDA	6.78E-4	-8.1E-4	0.392	-0.233	0.625	0.368, 0.17	5.25E-4, 4.13E-4	4.01E-11
FTO/FeMOF@PdNR/ PDA/antiMUC1Ab	4.78E-4	-6.1E-4	0.481	-0.231	0.712	0.425	3.45E-4	2.83E-11
FTO/FeMOF@PdNR/ PDA/antiMUC1Ab/MCH	5.67E-4	-7.4E-4	0.497	-0.257	0.754	0.487, 0.208	3.47E-4, 1.79E-4	3.36E-11

Electrochemical Detection of MUC1 using DPV technique

The DPV response of the biosensor surface (FTO/FeMOF@PDNR/PDA/antiMUC1ab/MCH) in the presence of MUC1 is shown in **figure S16a.** The MUC1 interaction results in reduction in peak current intensity owing to the hindered electron transfer rate. The slope of linear fit plot between the variation in current intensity and the log MUC1 concentration provided the detection limit (**Figure S16b**). Also, there is a spontaneous shift in the peak potential (towards lower potential) with the increase in MUC1 concentration on WE (**Figure S16c**). The LOD and LOQ are found to be 0.08 fg/ml and 0.26 fg/ml, respectively. The analytical sensitivity is calculated by dividing the slope (-2.53x10^{-5} A/fg mL^{-1}) of the sensor calibration curve by the electrode's surface area (0.175 cm^{-2}). The analytical sensitivity is found to be 14.45 x 10^{-5} A/fg ml^{-1}cm^{-2}.
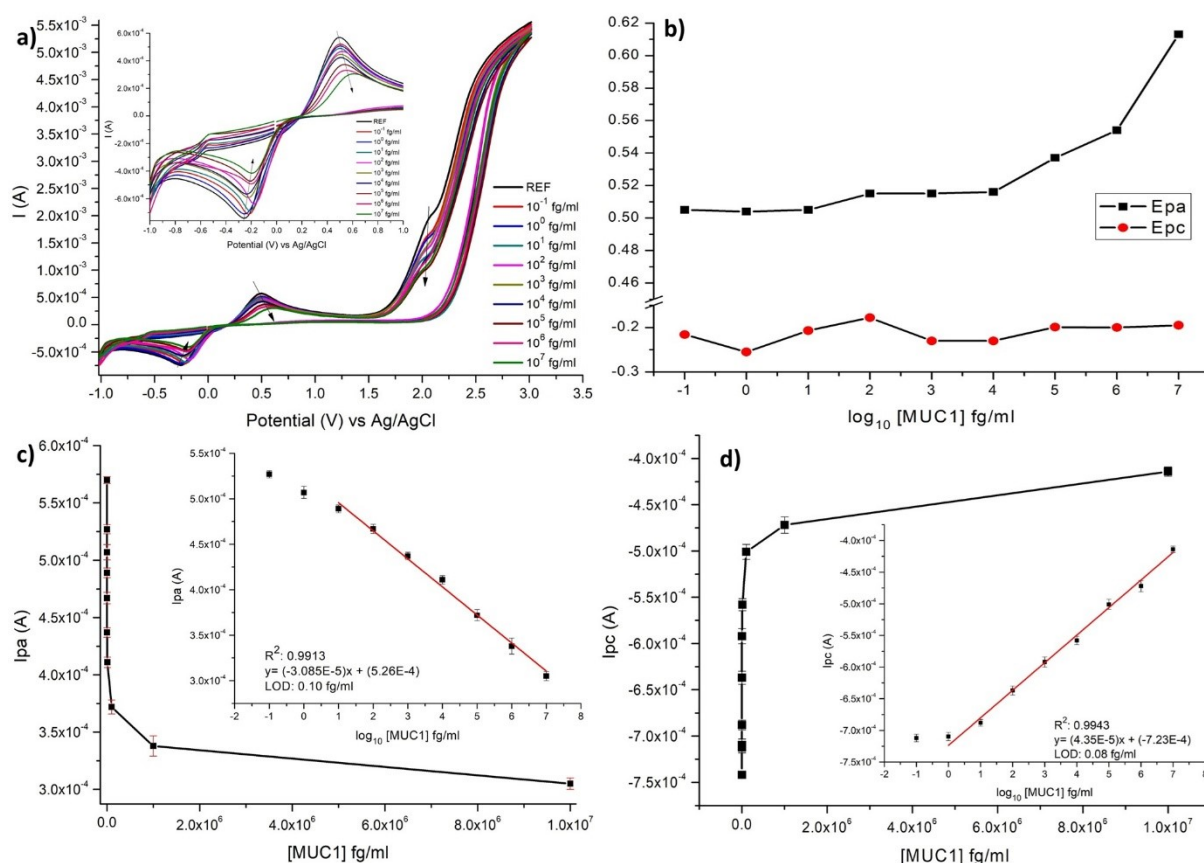
430
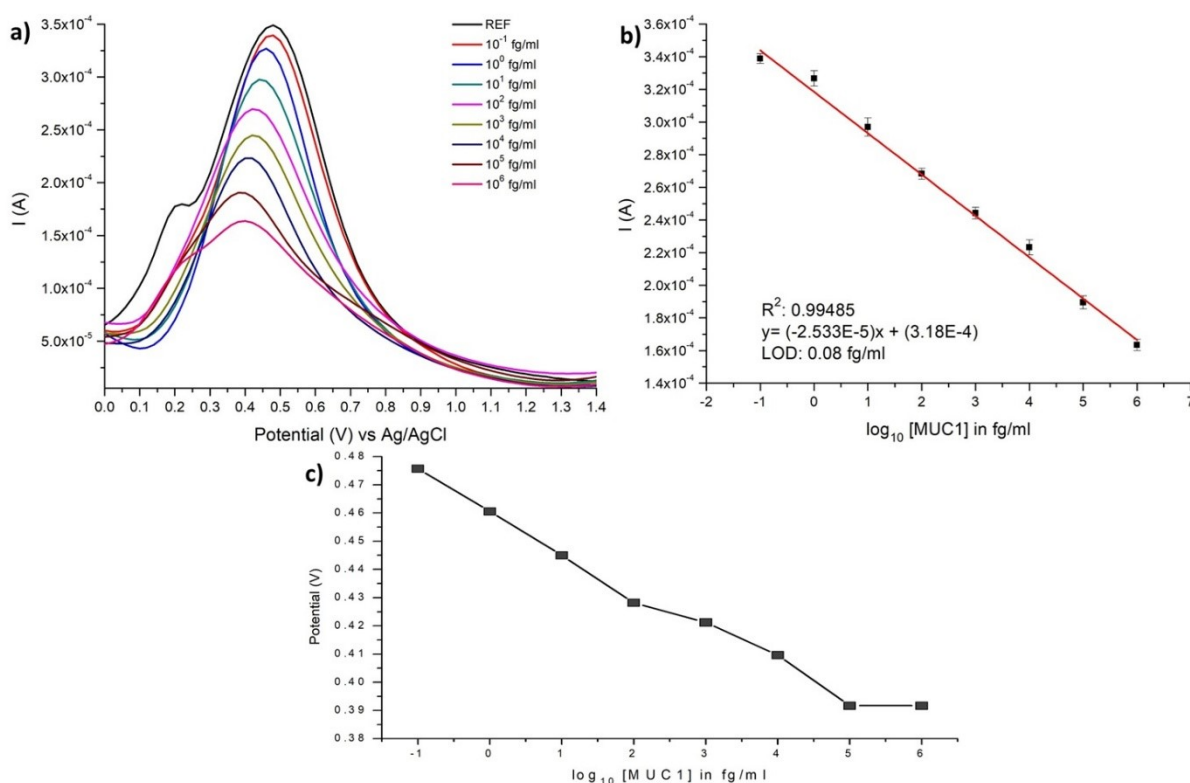
Figure S16: a) DPV response of immunosensor incubated with a range of MUC1 concentrations in buffer (reference represents the plot with only PBS), (b) the calibration plot drawn by assessing the variation of current (I in A) vs $\log_{10}$ [MUC1], and c) the variation in peak potential with the log MUC1 concentration increase.

Electrochemical Detection of MUC1 using CV technique

The cyclic voltametric measurements were performed with a step potential of 0.00244V, and a scan rate of 50 mV/s in PBS/KCl (pH 6) containing an equimolar concentration of 5 mM $K_3[Fe(CN)_6]/K_4[Fe(CN)_6]$. **Figure S17a** shows the CV response of the biosensor electrode (FTO/FeMOF@PdNR/PDA/antiMUC1Ab/MCH) in the presence of MUC1 at various concentrations. The gradual shift in the anodic peak potential, although unremarkable change in cathodic peak potential, clearly denotes that the MUC1-interaction substantially effects the oxidation reaction occurring at electrode/electrolyte interface (**Figure S17b**). The decrease in anodic and cathodic peak current concerning the increase in MUC1 concentration is evident in **figure S17c and S17d**, respectively. MUC1 binding to antiMUC1Ab resulted in partial blockage of electroactive sites on WE. The LOD is calculated from the linear fit plot of change in both the I_{pa} and I_{pc} concerning the log MUC1 concentration (**shown in insets of Figure S17c and S17d, respectively**). The as-calculated LOD are the 0.10 fg/ml and 0.08 fg/ml, respectively. The LOQ is found to be 0.37 fg/ml and 0.28 fg/ml, respectively. The analytical sensitivity is calculated by dividing the slope I_{pa} (-3.08 x10^{-5} A/fg mL^{-1}) and slope I_{pc} (4.35 x 10^{-5} A/fg mL^{-1}) of the sensor calibration curve by the electrode's surface area (0.175 cm^{-2}). The analytical sensitivity is found to be 17.6 x 10^{-5} A/fg ml^{-1}cm^{-2} and 24.85 x 10^{-5} A/fg ml^{-1}cm^{-2}.

From the **table S5,** it can be concluded that although both the impedance as well as the volumetric techniques provide the highly sensitive and accurate detection of MUC1 biomarker, using the proposed biosensor platform, but the variation in sensor's electrochemical properties is distinctively highly detectable in terms of impedance. The higher sensitivity of EIS compared to CV and DPV demonstrates that impedance is more effective at monitoring interfacial changes (charge transfer resistance) during biomolecular recognition.


Figure S17: a) CV response of immunosensor incubated with a range of MUC1 concentrations in buffer (reference represents the plot with only PBS), (b) the variation in anodic and cathodic peak potentials (E_{pa} and E_{pc}, respectively) with the log MUC1 concentration (fg/ml) increase, c) the calibration plot drawn by assessing the variation of current (I_{pa} in A) vs [MUC1] (fg/ml), and d) the calibration plot drawn by assessing the variation of current (I_{pc} in A) vs [MUC1] (fg/ml). [Inset of (a): the magnified CV response]; [Inset of (c): the linear fit plot of the variation in I_{pa} (A) vs $\log_{10}$ [MUC1] (fg/ml)]; [Inset of (d): the linear fit plot of the variation in I_{pc} (A) vs $\log_{10}$ [MUC1] (fg/ml)].

Selectivity

The selectivity of the developed biosensor was evaluated by comparing its response to MUC1 against other interfering molecules. The Nyquist plots, CV and DPV outputs (**Figure S18a-c, respectively**) of

the corresponding interactions presents a significantly higher impedance and lower current signal of FTO/FeMOF@PdNR/PDA/anti-MUC1Ab/MCH electrode after incubation with MUC1 as compared to other analytes such as HoloTC, BSA, insulin, hepcidin and MIX. In the case of the mixed sample (mix), a further increase in the Rct and decrease in current responses were observed, confirming that the biosensor could efficiently recognize the MUC1 even in the mixture.
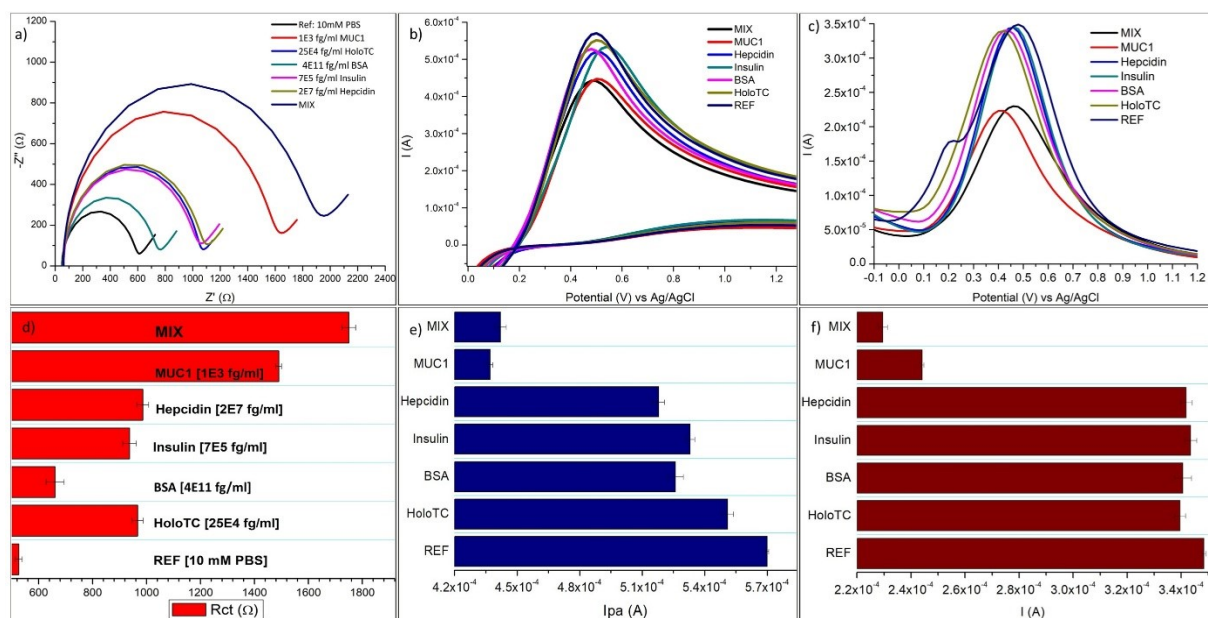
Figure S18: Selectivity analysis of the developed biosensor using EIS and voltammetry techniques. (a) Nyquist plots, b) I_{pa}, and c) DPV peak current, each comparing the biosensors response to MUC1 and other alone interfering molecules, HoloTC, BSA, insulin, and hepcidin, along with a mixed sample (MIX) and PBS as the reference; the corresponding d) Rct, e) I_{pa} (in A), and f) I (in A) values, demonstrating a significantly higher Rct and reduced current for MUC1 and the MIX, confirming the biosensor's high selectivity toward MUC1.

Comparative analysis of present study

The data in **table S5** shows that our biosensor presents the ultralow detection of MUC1 in terms of LOD (lower fg/ml) better than state-of-art (ng/ml to high fg/ml) range, in spiked human serum samples. Majority of the studies have not reported the analytical sensitivity, that shows a potential research gap, which is also addressed in the present study with outstanding analytical sensitivity, i.e., 1.39×10^3 Ω fg^{-1} mL cm^{-2}. Also, the present assay is rapid (with <2hr TOTAL assay time) while most of the assays require 14-24 hr. Furthermore, the wider linear range, spanning six orders of magnitude, exceeds the most reported ranges. The most crucial excellency of this biosensor lies in the multimodal validation (EIS, CV and DPV), this reinforces the robustness, and reliability of our sensing platform.

492 **Table S5:** The comparative analysis of the present biosensor electrode LOD, LOQ and analytical sensitivity with other reported studies for MUC1 detection.[2]

Working electrode Composition	Detection Technique	Sample Matrices	LOD	LOQ	Analytical Sensitivity	Total Assay Time	Linear range	Ref.
AuNPs@GCE	EIS, DPV	Human Serum	30 nM	100 nM		>21 hrs	1.0 μM	[20]
AuNPs@Cu$_7$S$_4$@Cu/Mn-AzoPPOP	DPV and CA	Spiked Serum	0.72 fg/ml, 0.82 fg/ml	2.4 & 2.7 fg/ml		-NA-	1-10^4 fg/ml	[21]
PEI-AuNPs	SWV	Human Serum	0.53 ng/ml	1.8 ng/ml		~1.5 hrs	0.1-10^2 ng/ml	[22]
GCE modified by CdTe/PPy	DPV	PBS	0.05 nM	0.16 nM	--	>15 hrs	0.1-10^2 nM	[23]
Cu-MOF/AuPtNPs	DPV	Human Serum	3.33 fM	11.1 fM		~23 hrs	10-10^7 fM	[24]
Au-PtBNPs@CGO/FTO	DPV	Spiked Human Serum	0.79 fM	2.63 fM		~2 hrs	1 fM-100 nM	[25]
AuNPs-GO-PEDOT	DPV	Spiked Serum	1 fg/ml (0.031 fM)	3.3 fg/ml		>24.25 hrs	3.13 aM- 31.2 nM	[26]
Ag-CuO integrated polyaniline	EIS	Spiked Serum	3.23 pg/ml	10.8 pg/ml	0.68 kΩ pg mL^{-1} cm^{-2}	~14.5 hrs	1-100 pg/ml	[27]
FTO/FeMOF@PdNR/ PDA/antiMUC1Ab /MCH	**EIS**	Human Serum	**0.074 fg/ml**	**0.24 fg/ml**	**1.39 x 10^3 Ω /fg ml^{-1}cm^{-2}**	**< 2 hrs**	**0.1-10^6 fg/ml**	**THIS WORK**
	CV (I$_{pa}$, I$_{pc}$)		**0.10 fg/ml, 0.08 fg/ml**	**0.37 fg/ml, 0.28 fg/ml**	**17.6 x 10^{-5} A/fg ml^{-1}cm^{-2}, 24.85 x 10^{-5} A/fg ml^{-1}cm^{-2}**			
	DPV		**0.08 fg/ml**	**0.26 fg/ml**	**14.45 x 10^{-5} A/fg ml^{-1}cm^{-2}**			

---

[2] GCE: Glassy carbon electrode; AuNP: Gold nanoparticles; PPOP: porphyrin-based porous organic polymers; CA: chrono-amperometry; PEI-AuNPs: polyethylenimine coated-gold nanoparticles, CdTe/PPy: cadmium telluride/polypyrrole, AuPtNPs; gold-platinum alloy nanoparticles, CGO: carboxylated graphene oxide, FTO: Fluorine-tin oxide, PEDOT: Poly(3,4-ethylenedioxythiophene; SWV: Square Wave Voltammetry; NA: non-assessable; PBS: Phosphate Buffer Saline;

Cost estimation

The approximate estimation of raw material cost, involved in this MUC1 biosensor, was performed to assess the economic viability. The fabrication cost of a single sensing electrode involves commonly available and low-cost components, including and FTO substrate (REUSABLE) (1 piece: ~0.3-0.5 USD); iron salts and organic ligands (μg scale: ~0.1 -0.2 USD) for FeMOF synthesis; palladium precursor (ng- μg: ~0.4- 0.6 USD) for PdNR, PDA (μl scale: ~<0.05 USD), EDC/NHS (μg scale: ~0.1-0.15 USD); anti-MUC1 Ab (ng scale: ~0.6-0.8 USD); and MCH (μl scale: ~<0.05 USD). Based on small batch lab-scale usage (in μg or ng scale for nanomaterials and Abs) and present commercial prices, the approximate raw material cost for fabricating one FTO/FeMOF@PdNR/PDA.antiMUC1Ab/MCH electrode is estimated to be in the range of ~USD 2-3. Importantly, this estimate corresponds to lab-scale fabrication, and is expected to further decrease substantially upon scale-up, batch synthesis of nanomaterials and bulk procurement of reagents. Moreover, the reusable FTO electrodes, drop-casting method, and absence of expensive enzymes or labels (label-free detection) further supports the cost-effectiveness of the proposed platform.

Rationale for using nanostructure-modified electrodes for antibody loading

In the **figure S19**, although the APTES-modified FTO surface exhibits a lower charge transfer resistance (R_{ct}) compared to FTO/FeMOF@PdNR/PDA electrode, the primary objective of a biosensor is not merely high conductivity but enhanced sensitivity towards target analyte. Notably, upon antibody functionalization, the increase in R_{ct} observed for the FTO/FeMOF@PdNR/PDA electrode is approx. three times higher than that of the FTO/APTES surface. This pronounced change in interfacial resistance indicates a substantially higher antibody loading capacity on the nanostructured FTO/FeMOF@PdNR/PDA platform. Consequently, the increased availability of active binding sites facilitates greater antigen capture, leading to amplified signal generation and superior biosensing sensitivity.

520
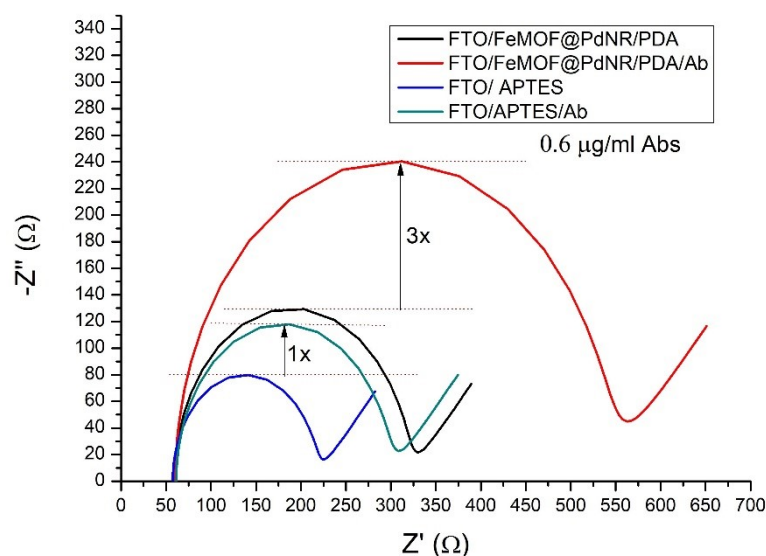
Figure S19: The effect of antibody (0.6 μg/ml) on the Rct value of APTES-modified and FeMOF@PdNR/PDA modified FTO surface.

References

1. Sheta, S.M., S.R. Salem, and S.M.J.J.o.M.R. El-Sheikh, *A novel Iron (III)-based MOF: Synthesis, characterization, biological, and antimicrobial activity study.* 2022. **37**(14): p. 2356-2367.
2. Wang, D. and Z. Li, *Coupling MOF-based photocatalysis with Pd catalysis over Pd@MIL-100(Fe) for efficient N-alkylation of amines with alcohols under visible light.* Journal of Catalysis, 2016. **342**: p. 151-157.
3. Sayyah, S., et al., *Chemical Polymerization Kinetics of Poly-O-Phenylenediamine and Characterization of the Obtained Polymer in Aqueous Hydrochloric Acid Solution Using K2Cr2O7 as Oxidizing Agent.* International Journal of Polymer Science, 2014. **2014**: p. 1-16.
4. Andris, S., et al., *Monitoring of antibody-drug conjugation reactions with UV/Vis spectroscopy.* J Biotechnol, 2018. **288**: p. 15-22.
5. Godfrey, H.G.W., et al., *Analysis by synchrotron X-ray scattering of the kinetics of formation of an Fe-based metal-organic framework with high CO2 adsorption.* APL Materials, 2019. **7**(11).
6. Coates, J., *Interpretation of Infrared Spectra, A Practical Approach*, in *Encyclopedia of Analytical Chemistry*.
7. Qin, W., et al., *Hydrothermal Synthesis and Characterization of Single‐Crystalline α‐Fe2O3 Nanocubes.* 2011. **2011**(1): p. 159259.
8. Parak, S., et al., *RSM optimization of biodiesel production by a novel composite of Fe (III)-based MOF and phosphomolybdic acid.* 2022. **48**(9): p. 3773-3793.
9. Bahari, A.J.J.o.S. and N. Magnetism, *Characteristics of Fe 3 O 4, α-Fe 2 O 3, and γ-Fe 2 O 3 nanoparticles as suitable candidates in the field of nanomedicine.* 2017. **30**: p. 2165-2174.
10. Yoon, C.-J., et al., *Fabrication of sustainable and multifunctional TiO2@carbon nanotube nanocomposite fibers.* Applied Surface Science, 2021. **541**: p. 148332.
11. Chen, D., et al., *Boosting Catalysis of Pd Nanoparticles in MOFs by Pore Wall Engineering: The Roles of Electron Transfer and Adsorption Energy.* 2020. **32**(30): p. 2000041.
12. Lin, A., et al., *Palladium nanoparticles supported on Ce-metal–organic framework for efficient CO oxidation and low-temperature CO2 capture.* 2017. **9**(21): p. 17961-17968.
13. Campaña Perilla, A.L., et al., *Characterization of Bimetallic Pd-Fe Nanoparticles Synthesized in Escherichia coli.* ACS Appl Bio Mater, 2024. **7**(12): p. 8573-8589.

553 14. Hadjiivanov, K.I., et al., *Power of infrared and Raman spectroscopies to characterize metal-*
554 *organic frameworks and investigate their interaction with guest molecules.* 2020. **121**(3): p.
555 1286-1424.
556 15. Devi, S., et al., *Nitrogen-doped carbon quantum dots conjugated isoreticular metal-organic*
557 *framework-3 particles based luminescent probe for selective sensing of trinitrotoluene*
558 *explosive.* 2020. **187**(9): p. 536.
559 16. López, J., et al., *Insights into the Stability and Activity of MIL-53(Fe) in Solar Photocatalytic*
560 *Oxidation Processes in Water.* 2021. **11**(4): p. 448.
561 17. Huang, H. and X. Wang, *Pd nanoparticles supported on low-defect graphene sheets: for use as*
562 *high-performance electrocatalysts for formic acid and methanol oxidation.* Journal of Materials
563 Chemistry, 2012. **22**(42): p. 22533-22541.
564 18. Onat, F.E., A. Akıllı, and H. Kamış, *Electrochemical polymerization of o-phenylenediamine in*
565 *the presence of metal salts: influence of Cu(NO3)2 and AgNO3 on spectroelectrochemical*
566 *properties and morphology.* Surface Science and Technology, 2025. **3**(1): p. 2.
567 19. Lazanas, A.C. and M.I.J.A.m.s.a. Prodromidis, *Electrochemical impedance spectroscopy─ a*
568 *tutorial.* 2023. **3**(3): p. 162-193.
569 20. Song, J., et al., *Development of electrochemical aptamer biosensor for tumor marker MUC1*
570 *determination.* 2017. **12**(6): p. 5618-5627.
571 21. Zhao, H., et al., *Label-free and dual-amplified electrochemical bioanalysis of MUC1 based on*
572 *an inorganic-organic polymer hybrid mimic peroxidase (AuNPs@ Cu7S4@ Cu/Mn-AzoPPOP)*
573 *and catalytic hairpin assembly.* 2021. **345**: p. 130332.
574 22. Kuntamung, K., J. Jakmunee, and K.J.J.o.M.C.B. Ounnunkad, *A label-free multiplex*
575 *electrochemical biosensor for the detection of three breast cancer biomarker proteins*
576 *employing dye/metal ion-loaded and antibody-conjugated polyethyleneimine-gold*
577 *nanoparticles.* 2021. **9**(33): p. 6576-6585.
578 23. Wang, J., C. Kan, and B.J.A.M. Jin, *Highly sensitive electrochemical biosensor for MUC1*
579 *detection based on DNA-functionalized CdTe quantum dots as signal enhancers.* 2024. **16**(45):
580 p. 7806-7815.
581 24. Li, Y., et al., *A sensitive electrochemical MUC1 sensing platform based on electroactive Cu-*
582 *MOFs decorated by AuPt nanoparticles.* 2020. **167**(8): p. 087502.
583 25. Bharti, A., et al., *An electrochemical aptasensor for analysis of MUC1 using gold platinum*
584 *bimetallic nanoparticles deposited carboxylated graphene oxide.* 2020. **1097**: p. 186-195.
585 26. Gupta, P., et al., *An electrochemical aptasensor based on gold nanoparticles and graphene*
586 *oxide doped poly (3, 4-ethylenedioxythiophene) nanocomposite for detection of MUC1.* 2018.
587 **813**: p. 102-108.
588 27. Kaur, A., et al., *Ag-CuO integrated polyaniline based impedimetric detection of cancer*
589 *biomarker MUC1.* 2023. **194**: p. 109266.

590

591

592

593